

# Network Estimation for Stationary Time Series

Madeline A. Shelley <sup>\*</sup>, Chiara Boetti <sup>†</sup>, Marina I. Knight\*, Matthew A. Nunes<sup>†</sup>

December 15, 2025

## Abstract

High-dimensional multivariate time series are common in many scientific and industrial applications, where the interest lies in identifying key dependence structure within the data for subsequent analysis tasks, such as forecasting. An important avenue to achieve this is through the estimation of the conditional independence graph via graphical models, although for time series data settings the underpinning temporal dependence can make this task challenging. In this article, we propose a novel wavelet domain technique that allows the data-driven inference of the (sparse) conditional independence graph of a high-dimensional stationary multivariate time series. By adopting the locally stationary wavelet modelling framework, we repose the estimation problem as a well-principled wavelet domain graphical lasso formulation. Theoretical results establish that our associated estimation scheme enjoys good consistency properties when determining sparse dependence structure in input time series data. The performance of the proposed method is illustrated using extensive simulations and we demonstrate its applicability on a real-world dataset representing hospitalisations of COVID-19 patients.

**Keywords:** Multivariate time series; graphical models; wavelets; network estimation.

## 1 Introduction

In the statistical literature, graphical models are powerful tools to capture key dependence structures within multivariate data through the conditional independence graph ( $\mathcal{CIG}$ ): given a collection of random variables, one wishes to assess the relationship between two variables, conditioned on the remaining variables. In the classical Gaussian graphical model literature, undirected graphs represent such dependencies among variables: each node is a variable, and the absence of an edge between two nodes encodes conditional independence between their corresponding variables given all other nodes (variables). For high-dimensional data, it is often desirable to impose sparsity in the graphical structure of the covariance (Friedman et al., 2008), as driven by applications in various settings, spanning genetics (Wille and Bühlmann, 2006), biology (Jordan, 2004; Ni et al., 2022), economics (Cerchiello and Giudici, 2016), neurosciences (Dyrba et al., 2020; Hinne et al., 2015), and environmental science

---

<sup>\*</sup>Department of Mathematics, University of York, UK

<sup>†</sup>Department of Mathematical Sciences, University of Bath, UK

(Engelke and Hitz, 2020). For comprehensive statistical reviews of graphical models, see e.g., Lauritzen (1996) and Maathuis et al. (2018).

Improvements in modern data collection methods have resulted in large multivariate time series being routinely collected across many fields. Consequently, the estimation of conditional independence structures in such data has received growing attention in recent years (Brillinger, 1996; Gibberd and Nelson, 2015a; Jung et al., 2015; Dahlhaus, 2000; Dallakyan et al., 2022). The work in this article is in particular motivated by the analysis of spatially-observed hospitalisations, namely time series representing COVID-19 ventilation bed occupancy rates at 81 hospitals across the UK from April 2020 to July 2021. In this context, it is of interest to model and e.g., forecast the data in order to inform staffing resource needs. The data show clear spatial and temporal dependence (see Figure 1), but due to the dimension of the multivariate time series, analysis is challenging without the use of sparse modelling frameworks (Nason et al., 2025). Thus, being able to identify the key dependencies within the data in a principled manner is a vital initial aspect of analysis.

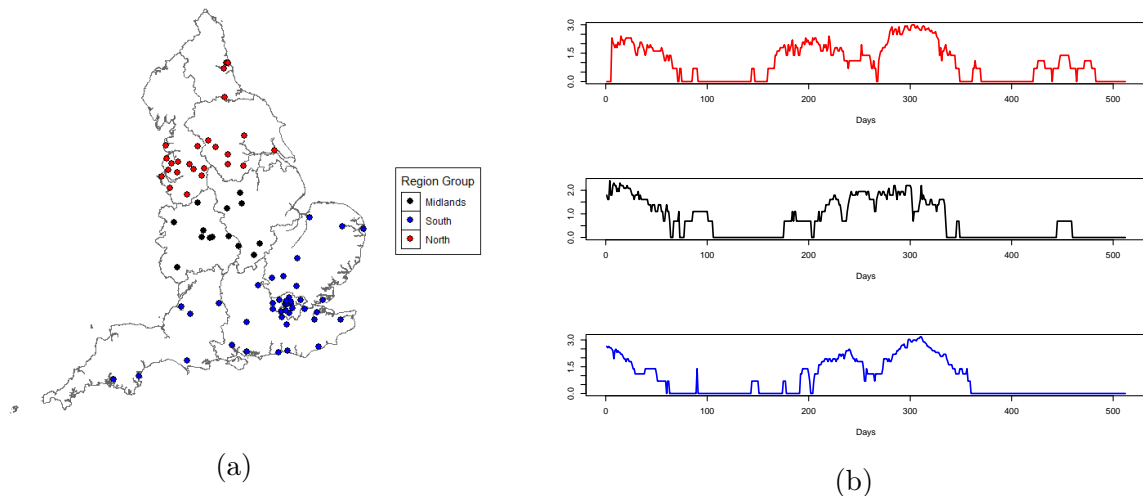


Figure 1: Illustration of the motivating COVID-19 hospitalisations dataset: (a) Locations of NHS Trusts with map split into geographical regions. Red indicates trusts in the North, black indicates trusts in the Midlands, and blue indicates trusts in the South; (b) Example COVID-19 time series: Airedale NHS Foundation Trust (red), Wye Valley NHS Trust (black), University Hospitals Plymouth NHS Trust (blue).

By direct analogy to the classical setting, the dependencies in multivariate time series processes are mapped onto the Fourier spectral domain (Brillinger, 1996; Dahlhaus, 2000). Specifically, missing edges in the  $\mathcal{CIG}$  correspond to zeros in the inverse spectral density (precision) matrix across all frequencies. Estimating the inverse spectral density matrix, however, poses significant challenges (Fiecas et al., 2019). A naive approach involves computing the smoothed periodogram—as it is a consistent estimator of the spectral density matrix—and subsequently inverting it. This strategy is suboptimal since the smoothed estimator often becomes ill-conditioned in high-dimensional settings or when the number of available observations is limited (Böhm and von Sachs, 2009). As a result, its inversion can severely amplify estimation errors, leading to inaccurate graphical structure inference.

These difficulties have motivated the development of two broad classes of regularized estimators. The first class of methods involves shrinking the spectral density matrix, either

before or after inversion (Fiecas et al., 2010; Fiecas and Ombao, 2011; Fiecas and von Sachs, 2014; Schneider-Luftman and Walden, 2016). While computationally straightforward, such techniques do not directly promote sparsity in the precision matrix, potentially obscuring the most informative conditional dependencies. The second class leverages the property that, for second-order stationary processes, the discrete Fourier coefficients at distinct frequencies are asymptotically independent and follow a complex-valued Gaussian distribution. This enables the extension of Gaussian graphical modelling frameworks to the frequency domain, yielding sparse and well-defined estimates of the precision matrix. We refer to this methodology as the *time series graphical lasso*. In this context, Jung et al. (2015) developed an estimation algorithm to learn the graphical dependence structure of time-dependent data. Later work extended this approach (Dallakyan et al., 2022; Tugnait, 2022) and studied related settings, including cases where the data exhibit long memory (Baek et al., 2023) or complex-valued time series models (Deb et al., 2024).

While these approaches naturally extend graphical models to time series, they all rely on the Fourier representation of the process. In this article we propose a wavelet domain approach to conditional independence graph estimation, motivated by the observation that wavelet-based time series decompositions can provide improvements over Fourier-based methods in a range of analysis tasks, even in the stationary time series setting. More precisely, we adopt the *locally stationary wavelet* (LSW) modelling framework introduced by Nason et al. (2000) and extended to the multivariate setting by Park et al. (2014), in which the wavelet spectral matrix captures process dependence through a time-scale representation of a multivariate time series.

Similar to Fourier-based methodology, the inverse of the wavelet spectrum matrices can be used for the inference of direct and indirect associations among the components of the process across both time and scale. Building on this, Gibberd and Nelson (2015b) introduced an algorithmic sparse estimation method for the inverse local wavelet spectrum based on an estimator of the spectrum; however, their work does not consider the true distributional properties of the wavelet coefficients associated to the process when finding an optimal inverse spectrum, leading to an unprincipled estimation scheme.

In this article we develop an alternative approach, the *wavelet-based time series graphical lasso* framework for multivariate stationary time series, by considering the wavelet precision matrix and properly accounting for the distributional properties associated to the spectral matrix estimator. Our methodology allows sparse estimation of the inverse wavelet spectra and aids the recovery of a multi-resolution decomposition of the conditional independence graph structure. Our proposed approach shows improved recovery of the true  $\mathcal{CIG}$  compared to both Fourier-based techniques in the literature and to the proposal of Gibberd and Nelson (2015b), particularly for challenging setups.

In addition to estimation of the  $\mathcal{CIG}$  for stationary time series, we also develop a tool for identifying the underlying graph, or network, in so-called network time series models. Originally proposed by Knight et al. (2016), Generalized Network Autoregressive (GNAR) processes model autoregressive dynamics while explicitly exploiting inter-dependencies encoded by a given graph,  $\mathcal{N} = (\mathcal{K}, \mathcal{E}^{\mathcal{N}})$ , via nodal neighbourhoods (subsets of  $\mathcal{K}$ ) as determined through the presence / absence of edges in  $\mathcal{E}^{\mathcal{N}}$ . Focusing on relevant connections was shown to improve parameter estimation and forecasting accuracy, as well as to enhance computational efficiency (Knight et al., 2020). However, when the underlying graph is unknown (i.e., unknown edge set  $\mathcal{E}^{\mathcal{N}}$ ), determining it from the data is a crucial first modelling task (Jiménez-Varón and Knight, 2025). One way to approach this issue is to fit network time

series models on several candidate graphs and to select the one with the smallest prediction error (Knight et al., 2020). This strategy, however, identifies a graph that aids prediction, which may differ from the graph that best represents the data-generating structure. Hence in this work we also propose a data-driven procedure that infers the graph  $\mathcal{N}$  directly from the dependence structure  $\mathcal{CIG}$  estimated by our wavelet-based time series graphical lasso, by means of an edge-clustering approach.

This article is organised as follows. Section 2 introduces the time series graphical lasso approach based on Fourier decomposition and provides an overview of the multivariate locally stationary process model of Park et al. (2014) upon which we build our proposed wavelet-based  $\mathcal{CIG}$  recovery methodology. Our proposed wavelet-based time series graphical lasso (to which we shall refer under the acronym WavTSglasso) is described in Section 3, which also addresses its related theoretical properties. We demonstrate the efficacy of our estimation procedure by extensive simulation studies in Section 4, while Section 5 proposes the discovery of the underlying graph for GNAR-type models via edge-wise clustering. Finally, Section 6 presents an application to a real dataset regarding COVID-19 patients hospitalisations, and illustrates the benefit of using the data-driven discovered network in a forecasting task.

## 2 Background

In this section, we review the time series graphical lasso (TSglasso) for multivariate stationary time series as developed by Jung et al. (2015), as well as giving a brief overview of multivariate locally stationary wavelet processes (Park et al., 2014). These two aspects provide the necessary background to formulate our proposed modelling framework in Section 3.

In what follows, we consider a  $P$ -dimensional, zero-mean stationary Gaussian process  $\mathbf{X} = \{\mathbf{X}_t\}_{t=0}^{T-1}$ , where  $\mathbf{X}_t = (X_t^{(1)}, \dots, X_t^{(P)})^\top$  is observed at time  $t$  across  $P$  channels.

Our aim is to characterise the interactions among the  $P$  components of the process  $\mathbf{X}$  by means of its underlying conditional independence graph  $\mathcal{CIG} = (\mathcal{K}, \mathcal{E})$ , with node set  $\mathcal{K} = \{1, \dots, P\}$  and undirected edge set  $\mathcal{E} = \{(p, q) \in \mathcal{K} \times \mathcal{K}, p \neq q : p \rightsquigarrow q\}$ , where the edge  $p \rightsquigarrow q$  indicates conditional dependence between channels  $p$  and  $q$ . In particular, we denote by  $\mathbf{G}$  the  $P \times P$ -dimensional adjacency matrix of the  $\mathcal{CIG}$ , with entries  $\mathbf{G}_{p,q} = 1$  if  $(p, q) \in \mathcal{E}$ , and  $\mathbf{G}_{p,q} = 0$  otherwise. By definition,  $\mathbf{G}$  is symmetric with zeros on the diagonal.

The  $\mathcal{CIG}$  can be determined from the process spectral properties, as follows. Let  $\mathbf{f}(\omega) \in \mathbb{C}^{P \times P}$  be the spectral density matrix of  $\mathbf{X}$  at frequency  $\omega \in [0, 1]$ , and consider the precision matrix function  $\mathbf{Q}(\omega) := \mathbf{f}^{-1}(\omega)$ . Dahlhaus (2000) shows that the channel  $p, q$  processes,  $\{X_t^{(p)}\}$  and  $\{X_t^{(q)}\}$ , are independent conditional on all remaining components if and only if  $\mathbf{Q}_{p,q}(\omega) = 0, \forall \omega$ , thus rendering a bijective characterisation of the edge set  $\mathcal{E}$ .

### 2.1 Fourier-based Time Series Graphical Lasso (TSglasso)

Let us now consider the task of estimation of the conditional dependencies in the data. Denote the  $P$ -dimensional Fourier coefficients of  $\mathbf{X}$  by  $\{\mathbf{d}(\omega_n)\}_{n=0}^{T-1}$ , obtained by applying the normalised discrete Fourier transform to  $\mathbf{X}$ , where  $\omega_n = \frac{n}{T}$ . Under the assumption that  $\mathbf{X}$  has an absolutely summable autocovariance function, Brillinger (2001) showed that, as  $T \rightarrow \infty$ ,  $\mathbf{d}(\omega_n) \sim N_P^{\mathbb{C}}(\mathbf{0}, \mathbf{f}(\omega_n))$  independently for  $n = 1, \dots, \lfloor \frac{T}{2} \rfloor - 1$ . Moreover, for  $n = 0, \lfloor \frac{T}{2} \rfloor$ , we have  $\mathbf{d}(\omega_n) \sim N_P(\mathbf{0}, \mathbf{f}(\omega_n))$  though these coefficients are typically ignored. Here, the notations

$\sim N_P^{\mathbb{C}}$  and  $\sim N_P$  indicate that the variables are approximately distributed as complex- and real-valued Gaussian, respectively.

Using standard Fourier spectral estimation that employs local periodogram smoothing over  $M$  consecutive aggregated frequencies  $\tilde{\omega}_l = \frac{(l-1)L+m_t+1}{T}$  for  $l = 1, \dots, M$ , with  $M = \lfloor \frac{T/2-m_t-1}{L} \rfloor$  the number of frequencies after smoothing, half-window length  $m_t$ , and  $L = 2m_t+1$ , then the smoothed sample spectral density is defined as

$$\tilde{\mathbf{f}}(\tilde{\omega}_l) = \frac{1}{L} \sum_{k=-m_t}^{m_t} \mathbf{d}(\tilde{\omega}_{l,k}) \mathbf{d}^H(\tilde{\omega}_{l,k}),$$

with  $\tilde{\omega}_{l,k} = \frac{(l-1)L+m_t+1+k}{T}$ ,  $k = -m_t, \dots, m_t$ , denoting the  $L$  disjoint frequencies in the  $l$ -th window, and  $\cdot^H$  denoting the Hermitian transpose.

As usual in the time series Fourier spectral domain literature, following from the (complex-valued) Gaussian distributions of the Fourier coefficients and the sample spectral density matrix above, the log-likelihood function for the precision matrix  $\mathbf{Q}(\cdot)$  can be written as

$$\mathcal{L}(\mathbf{Q}(\cdot)) = \sum_{l=1}^M L \left[ \log \det(\mathbf{Q}(\tilde{\omega}_l)) - \text{tr} \left( \tilde{\mathbf{f}}(\tilde{\omega}_l) \mathbf{Q}(\tilde{\omega}_l) \right) \right], \quad (1)$$

and in the spirit of the graphical lasso, a sparse estimator  $\hat{\mathbf{Q}}(\cdot)$  may be obtained by solving the regularised optimisation problem

$$\min_{\mathbf{Q}(\cdot)} \{ -\mathcal{L}(\mathbf{Q}(\cdot)) + \mathcal{P}(\mathbf{Q}(\cdot), \lambda) \}, \quad (2)$$

where in the above equations  $\mathcal{P}(\mathbf{Q}(\cdot), \lambda)$  is a sparsity inducing penalty function and  $\text{tr}(\mathbf{A})$  denotes the trace operator applied to the matrix  $\mathbf{A}$ . For example, [Jung et al. \(2015\)](#) use an  $\ell_1$ -penalty, [Tugnait \(2022\)](#) defines a sparse group penalty, whilst [Dallakyan et al. \(2022\)](#) explore an  $\ell_2$ -penalty in a two-stage sparse estimation procedure for vector autoregressive processes. The optimisation problem (2) is typically solved using the alternating direction method of multipliers (ADMM) ([Boyd et al., 2011](#)), exploiting variable splitting and the separability of the objective function across frequencies  $\{\tilde{\omega}_l\}_{l=1}^M$ . Because  $\mathbf{Q}(\cdot)$  is complex-valued, Wirtinger calculus is used to derive suitable ADMM update steps while incorporating the assumption of smooth variation across nearby frequencies ([Dallakyan et al., 2022](#)). This translates into choosing an appropriate smoothing span  $L$  in (1).

A further step in the TSglasso framework is how to infer the adjacency matrix  $\mathbf{G}$  from the estimated precision matrix functions. Indeed, note that solving (2) yields  $M$  estimates, i.e.,  $\hat{\mathbf{Q}}(\tilde{\omega}_l) \in \mathbb{C}^{P \times P}$  for all  $\tilde{\omega}_l$  for  $l = 1, \dots, M$ . Techniques in the literature aggregate these estimates in different ways to form an estimated adjacency,  $\hat{\mathbf{G}}$ . For example, [Dallakyan et al. \(2022\)](#) set  $\hat{\mathbf{G}}_{p,q} = 0$ , i.e., no edge between nodes  $p$  and  $q$ , iff  $\hat{\mathbf{Q}}_{p,q}(\tilde{\omega}_l) = 0$  for all  $l$ . However, this approach can reduce sparsity: small nonzero entries at some frequencies will still result in edges in the final graph. As an alternative, [Tugnait \(2022\)](#) determines the presence of an edge between the  $p$ -th and  $q$ -th in the  $\mathcal{CIG}$  if the  $\ell_2$ -norm of the vector  $(\hat{\mathbf{Q}}_{p,q}(\tilde{\omega}_1), \dots, \hat{\mathbf{Q}}_{p,q}(\tilde{\omega}_M))$  is different from zero.

To preserve sparsity, in our TSglasso implementation we summarise the  $M$  estimates using the entrywise  $\ell_1$ -norm for each  $p, q = 1, \dots, P$ ,

$$\overline{\mathbf{Q}}_{p,q} = \frac{1}{M} \sum_{l=1}^M |\hat{\mathbf{Q}}_{p,q}(\tilde{\omega}_l)|,$$

where  $\overline{\mathbf{Q}} \in \mathbb{R}^{P \times P}$  is the resulting matrix. We then form  $\hat{\mathbf{G}}$  by setting the corresponding entries to 1 where  $\overline{\mathbf{Q}}$  is non-zero. In practice, to account for numerical noise, we set  $\hat{\mathbf{G}}_{p,q} = 0$  if  $|\overline{\mathbf{Q}}_{p,q}| < c$ , where we use  $c = 10^{-5}$  as in [Dallakyan et al. \(2022\)](#).

**Tuning Parameter Selection.** The parameter  $\lambda$  of the penalty term  $\mathcal{P}(\mathbf{Q}(\cdot), \lambda)$  in the TSglasso problem (2) controls the sparsity of the estimated precision matrix  $\mathbf{Q}(\cdot)$ . Traditionally,  $\lambda$  is selected by minimizing the Akaike Information Criterion (AIC) ([Akaike, 1974](#)), the Bayesian Information Criterion (BIC) ([Schwarz, 1978](#)), or the extended Bayesian Information Criterion (eBIC) ([Chen and Chen, 2008](#)). An alternative is cross-validation (CV), as suggested by [Matsuda et al. \(2006\)](#), however, we do not use it in this work since it is more computationally expensive and it underperforms when compared to information criteria in practical tasks.

By denoting the frequency-specific terms  $\mathcal{L}(\mathbf{Q}(\tilde{\omega}_l)) := \log \det(\mathbf{Q}(\tilde{\omega}_l)) - \text{tr}(\tilde{\mathbf{f}}(\tilde{\omega}_l)\mathbf{Q}(\tilde{\omega}_l))$  in (2) for each  $l$ , [Tugnait \(2022\)](#) and [Dallakyan et al. \(2022\)](#) define the BIC as

$$\text{BIC}(\lambda) = -2L \sum_{l=1}^M \mathcal{L}(\mathbf{Q}(\tilde{\omega}_l)) + \log(2LM) \sum_{l=1}^M E_l,$$

where  $E_l$  is the number of non-zero elements in  $\mathbf{Q}(\tilde{\omega}_l)$ . Similarly, the AIC and eBIC ([Dallakyan et al., 2022](#)) are

$$\text{AIC}(\lambda) = -2L \sum_{l=1}^M \mathcal{L}(\mathbf{Q}(\tilde{\omega}_l)) + 2LM \sum_{l=1}^M E_l,$$

and

$$\text{eBIC}(\lambda) = -2L \sum_{l=1}^M \mathcal{L}(\mathbf{Q}(\tilde{\omega}_l)) + \log(2LM) \sum_{l=1}^M E_l + 4\gamma \log(P) \sum_{l=1}^M E_l,$$

where  $\gamma \in [0, 1]$  is an additional hyper-parameter.

## 2.2 Multivariate Locally Stationary Wavelet Processes

Although the process under consideration in this work is assumed to be stationary, we shall employ the locally stationary wavelet (LSW) modelling framework of [Nason et al. \(2000\)](#) to allow for projections into the wavelet spectral domain. This framework has found a variety of applications across fields such as biology ([Hargreaves et al., 2018](#)), neuroscience ([Embleton et al., 2022; Knight et al., 2024](#)), healthcare ([Del Angel et al., 2025](#)) and economics ([Killick et al., 2020, 2024](#)). [Park et al. \(2014\)](#) propose an extension, the *multivariate locally stationary wavelet* (mvLSW) model for the process  $\mathbf{X} = \{\mathbf{X}_t\}_{t=0}^{T-1}$ , with  $T = 2^J$  and  $J \in \mathbb{N}$ , which allows for time-varying dependence within and across channels of the multivariate time series. The model expresses the process as a superposition of discrete non-decimated wavelets across scales  $j$  and times  $k$

$$\mathbf{X}_t = \sum_{j=1}^{\infty} \sum_{k \in \mathbb{Z}} \mathbf{V}_j(k/T) \psi_{j,t-k} \boldsymbol{\varepsilon}_{j,k},$$

where  $\{\psi_{j,t-k}\}_{j,k}$  is a set of non-decimated wavelets at scale  $j$  and location  $k$ ,  $\mathbf{V}_j(u)$  is the scale  $j$  transfer function matrix at rescaled time  $u = k/T \in [0, 1]$ , and  $\{\boldsymbol{\varepsilon}_{j,k}\}_{j,k}$  are uncorrelated  $P$ -dimensional random vectors with zero mean and identity covariance matrix. Each  $\mathbf{V}_j(\cdot)$

is assumed to have a lower-triangular matrix form, whose entries are Lipschitz continuous functions with Lipschitz constant  $L_j^{(p,q)}$  satisfying  $\sum_{j=1}^{\infty} 2^j L_j^{(p,q)} < \infty$ . For clarity, here we use the indexing convention that small  $j$  corresponds to fine levels, and large  $j$  to coarse scales.

The *local wavelet spectral* (LWS) matrix function  $\mathbf{S}_j(u) \in \mathbb{R}^{P \times P}$  yields a time-scale decomposition of the process power at each scale  $j$  and rescaled time  $u$ , and it is defined as

$$\mathbf{S}_j(u) = \mathbf{V}_j(u) \mathbf{V}_j(u)^\top.$$

The LWS function is connected to the (localised) cross-channel covariance between channels  $p$  and  $q$  of  $\mathbf{X}$ , as

$$\text{Cov}(X_{\lfloor uT \rfloor, T}^{(p)}, X_{\lfloor uT \rfloor + \tau, T}^{(q)}) \approx c^{(p,q)}(u, \tau) = \sum_{j=1}^{\infty} S_j^{(p,q)}(u) \Psi_j(\tau), \quad (3)$$

where  $\Psi_j(\tau) = \sum_k \psi_{j,k} \psi_{j,k-\tau}$  is the discrete autocorrelation wavelet (Nason et al., 2000), and  $\approx$  denotes equality up to an  $\mathcal{O}(T^{-1})$  factor (Park et al., 2014).

Note the LWS is a real-valued continuous function defined on the rescaled time domain  $[0, 1]$ ; since in practice, we only observe the process at discrete time points  $k = \lfloor uT \rfloor$  with  $k = 0, \dots, T-1$ , the notation  $\mathbf{S}_{j,k} = \mathbf{S}_j(k/T)$  is often adopted (Park et al., 2014). In this vein, denote the precision matrix function as  $\Theta_j(u) := \mathbf{S}_j^{-1}(u)$ .

Let  $\mathbf{d}_{j,k} = (d_{j,k}^{(1)}, \dots, d_{j,k}^{(P)})^\top$  be the empirical wavelet coefficient vector, defined as

$$\mathbf{d}_{j,k} = \sum_{t=0}^{T-1} \mathbf{X}_t \psi_{j,k}(t),$$

and let  $\mathbf{I}_{j,k} = \mathbf{d}_{j,k} \mathbf{d}_{j,k}^\top$  be the wavelet matrix periodogram. Then, Park et al. (2014) define an asymptotically unbiased estimator of  $\mathbf{S}_{j,k}$  for each  $j$  and each  $k$  as

$$\hat{\mathbf{S}}_{j,k} := \sum_{l=1}^J (\mathbf{C}^{-1})_{jl} \tilde{\mathbf{I}}_{l,k}, \quad (4)$$

where  $J = \log_2(T)$ ,  $\tilde{\mathbf{I}}_{l,k}$  is the wavelet periodogram, smoothed across time to achieve consistency, and  $\mathbf{C}$  is the discrete autocorrelation wavelet inner product matrix, with  $C_{jl} = \langle \Psi_j, \Psi_l \rangle$  (Park et al., 2014).

Gibberd and Nelson (2015b) propose introducing sparsity in the inverse local wavelet spectrum,  $\Theta_{j,k} := \mathbf{S}_{j,k}^{-1}$ , at each scale  $j$  and location  $k$  by means of the following  $\ell_1$ -regularised optimisation

$$\hat{\Theta}_{j,k} := \arg \min_{\Theta \succeq 0} \left\{ -\log \det(\Theta) + \text{tr}(\hat{\mathbf{S}}_{j,k} \Theta) + \lambda_j \|\Theta\|_1 \right\}. \quad (5)$$

Although it is reasonable to assume that the wavelet coefficients are zero-mean Gaussian and uncorrelated across locations  $k$  within each scale  $j$ , as shown in Park et al. (2014), the expectation of the raw wavelet periodogram  $\mathbf{I}_{j,k}$  satisfies

$$\mathbb{E}(\mathbf{I}_{j,k}) \approx \sum_{l=1}^J C_{jl} \mathbf{S}_l(k/T) = \boldsymbol{\beta}_j(k/T) =: \boldsymbol{\beta}_{j,k}. \quad (6)$$

Since  $\mathbb{E}(\mathbf{d}_{j,k}) = \mathbf{0}$  due to the zero-mean definition of the random increments  $\{\boldsymbol{\varepsilon}_{j,k}\}_{j,k}$ , the above implies  $\mathbf{d}_{j,k} \sim N_P(\mathbf{0}, \boldsymbol{\beta}_{j,k})$ , so that the actual inverse covariance matrix of the wavelet

coefficients is  $\beta_{j,k}^{-1}$ . This is in contrast to the one employed in the optimisation problem (5), namely  $\mathbf{S}_{j,k}^{-1}$ , thus illustrating how this formulation does not correctly account for the true distribution of the wavelet coefficients. Under the process stationarity assumption, we next propose a principled way to bypass this problem.

### 3 Proposed Wavelet-based Time Series Graphical Lasso

In what follows we show that under the assumption of process stationarity, we can characterise the adjacency matrix of the  $\mathcal{CIG}$  in the [Dahlhaus \(2000\)](#) sense by the corresponding adjacency matrix formed from the scale-dependent wavelet precision matrices,  $\{\Theta_j := \mathbf{S}_j^{-1}\}_j$ , where under stationarity, we drop the time-localisation typical of LSW processes. This characterisation then becomes central to our proposal for wavelet-based  $\mathcal{CIG}$  estimation.

**Proposition 1.** *Let  $\mathbf{X} = \{\mathbf{X}_t\}_{t=0}^{T-1}$  be a  $P$ -dimensional, zero-mean stationary Gaussian process, where  $\mathbf{X}_t = (X_t^{(1)}, \dots, X_t^{(P)})^\top$  is observed at time  $t$  across  $P$  channels (nodes). Assume that the process  $\mathbf{X}$  admits a multivariate locally stationary wavelet representation as in [Park et al. \(2014\)](#) whose spectral structure we denote as  $\{\mathbf{S}_j\}_j$  across the scales  $j = 1, \dots, J = \log_2(T)$ .*

*Then the conditional independence of two nodes  $p$  and  $q$  may be characterised at each scale  $j$  through the presence of a zero-valued entry in the corresponding wavelet precision matrix, i.e.  $(\Theta_j)_{p,q} = (\mathbf{S}_j^{-1})_{p,q} = 0$ .*

The proof appears in Appendix A.1 and makes use of the Fourier spectral domain characterisation typically used in graphical modelling ([Dahlhaus, 2000](#)) applied to scale-dependent subprocesses defined akin to [Wu et al. \(2023\)](#).

#### 3.1 Scale-based $\mathcal{CIG}$ Estimation

Following the arguments in Section 2.2 and recalling process Gaussianity and stationarity, at each scale  $j$  the wavelet coefficients of the stationary process  $\mathbf{X}$  are zero-mean  $P$ -dimensional Gaussian random vectors with covariance matrix  $\beta_j(k/T) = \beta_j$  for every time  $k$ , or equivalently,  $\mathbf{d}_{j,k} \sim N_P(\mathbf{0}, \beta_j)$  for  $k = 0, \dots, T-1$ . As discussed in Section 2, the distributional properties of the discrete Fourier coefficients were exploited to formulate a sparse estimation problem for the inverse spectral density matrix function. In contrast, the discrete wavelet coefficients yield the quantities  $\beta_j$ —linear combinations of the  $\mathbf{S}$ -spectra, as shown in equation (6)—and cannot be directly used instead of  $\mathbf{S}_j$ .

Explicitly, the joint probability distribution of the wavelet coefficients  $\{\mathbf{d}_{j,k}\}_k$  at scale  $j$  is

$$p(\mathbf{d}_{j,0}, \dots, \mathbf{d}_{j,T-1}) = \prod_{k=0}^{T-1} \frac{1}{\pi^P} (\det(\beta_j))^{-1} \exp\{-\mathbf{d}_{j,k}^T \beta_j^{-1} \mathbf{d}_{j,k}\},$$

and hence the log-likelihood expressed in terms of  $\boldsymbol{\beta}_j^{-1}$  can be derived as

$$\begin{aligned}\mathcal{L}(\boldsymbol{\beta}_j^{-1}) &= \sum_{k=0}^{T-1} [\log \det(\boldsymbol{\beta}_j^{-1}) + \text{tr}(-\mathbf{d}_{j,k} \mathbf{d}_{j,k}^T \boldsymbol{\beta}_j^{-1})] \\ &= T \log \det(\boldsymbol{\beta}_j^{-1}) - \sum_{k=0}^{T-1} \text{tr}(\mathbf{I}_{j,k} \boldsymbol{\beta}_j^{-1}) \\ &= T [\log \det(\mathbf{B}_j) - \text{tr}(\bar{\mathbf{I}}_j \mathbf{B}_j)],\end{aligned}$$

where  $\bar{\mathbf{I}}_j = \frac{1}{T} \sum_{k=0}^{T-1} \mathbf{I}_{j,k}$  and  $\mathbf{B}_j := \boldsymbol{\beta}_j^{-1}$ . Note here that smoothing over the entire time domain is used for the periodogram since  $\mathbf{X}$  is a stationary process. Hence, in the wavelet context an optimisation problem akin to (2) would be given by

$$\hat{\mathbf{B}}_j = \arg \min_{\mathbf{B}_j} \left\{ -T [\log \det(\mathbf{B}_j) - \text{tr}(\bar{\mathbf{I}}_j \mathbf{B}_j)] + \mathcal{P}(\mathbf{B}_j, \lambda) \right\}, \quad (7)$$

where  $\mathcal{P}(\mathbf{B}_j, \lambda) = \lambda \sum_{p \neq q} |(\mathbf{B}_j)_{p,q}|$ . Observe the evident multiresolution aspect, resulting in a separate optimisation problem for each scale  $j$ . Also, note that in this setup, the penalty term encourages sparsity by forcing zeros in the off-diagonal entries of the inverse  $\boldsymbol{\beta}$ -spectrum. Consequently, any optimisation problem we consider directly deriving from the *wavelet* coefficients is written in terms of the  $\boldsymbol{\beta}$ -spectra, with the penalty enforcing sparsity in  $\boldsymbol{\beta}_j^{-1}$  rather than in the target  $\mathbf{S}_j^{-1}$ , in contrast to the formulation in (5). This mismatch between the  $\boldsymbol{\beta}$ - and  $\mathbf{S}$ -spectra is a well-known issue (see e.g. [Knight et al. \(2024\)](#)) and must be handled carefully depending on the context; we address this aspect next.

We begin by considering an approach that allows us to enforce sparsity directly in the precision matrix,  $\mathbf{S}_j^{-1}$ , while still using the distributional properties of the wavelet coefficients. We propose to *define a new process*  $\mathbf{Y} = \{\mathbf{Y}_t\}_{t=0}^{T-1}$ , with corresponding wavelet coefficients  $\{\mathbf{d}_{j,k}^{(Y)}\}_{j,k}$ , whose covariance matrices  $\{\boldsymbol{\beta}_j^{(Y)}\}_j$  are designed to match  $\{\mathbf{S}_j^{(X)}\}_j$ . Indeed, this would allow us to reformulate the optimisation problem (7) in terms of the precision matrix  $\boldsymbol{\Theta}_j^{(X)} := (\mathbf{S}_j^{(X)})^{-1}$ , and therefore to estimate the  $\mathcal{CIG}$  of the process  $\mathbf{X}$  on a *scale-by-scale basis*. Note we now use the superscript  $(\cdot)$  to explicitly indicate the process.

To this end, our proposal is to simulate the new process  $\mathbf{Y}$  such that its spectral structure is given by  $\{\mathbf{S}_j^{(Y)}\}_j$ , where  $\mathbf{S}_j^{(Y)} = \sum_{l=1}^J (\mathbf{C}^{-1})_{jl} \mathbf{S}_l^{(X)}$ ,  $\forall j$ . Then, using equation (6) for the wavelet coefficients associated to the new process  $\mathbf{Y}$ , we obtain at each scale  $j$ ,

$$\mathbb{E} \left( \mathbf{d}_{j,k}^{(Y)} \left( \mathbf{d}_{j,k}^{(Y)} \right)^\top \right) \approx \mathbf{S}_j^{(X)}, \quad (8)$$

which leads us to  $\mathbf{d}_{j,k}^{(Y)} \sim N_P(\mathbf{0}, \mathbf{S}_j^{(X)})$ ,  $\forall k$ , as desired. The  $(p, q)$  component in equation (8) arises from the following relationship between the  $J$ -dimensional vectors that collate the  $\boldsymbol{\beta}$ - and  $\mathbf{S}$ -spectra for each channel pair  $(p, q)$ , such that

$$\left( (\boldsymbol{\beta}_j^{(Y)})_{p,q} \right)_{j=1}^J = \mathbf{C} \left( (\mathbf{S}_j^{(Y)})_{p,q} \right)_{j=1}^J = \mathbf{C}(\mathbf{C}^{-1}) \left( (\mathbf{S}_j^{(X)})_{p,q} \right)_{j=1}^J = \left( (\mathbf{S}_j^{(X)})_{p,q} \right)_{j=1}^J.$$

This reveals the rationale behind our proposal to use the *new process* wavelet coefficients,  $\{\mathbf{d}_{j,k}^{(Y)}\}_k$ , to enforce sparsity in the original precision  $\boldsymbol{\Theta}_j^{(X)}$  within each scale  $j$ . Specifically,

we propose to formulate *at each scale  $j$*  an optimisation problem akin to equation (7),

$$\hat{\Theta}_j^{(X)} = \arg \min_{\Theta_j^{(X)}} \left\{ -T \left[ \log \det \left( \Theta_j^{(X)} \right) - \text{tr} \left( \bar{\mathbf{I}}_j^{(Y)} \Theta_j^{(X)} \right) \right] + \mathcal{P} \left( \Theta_j^{(X)}, \lambda_j \right) \right\}, \quad (9)$$

where we use  $\bar{\mathbf{I}}_j^{(Y)} = \frac{1}{T} \sum_{k=0}^{T-1} \mathbf{I}_{j,k}^{(Y)}$ , the time-averaged periodogram of the process  $\mathbf{Y}$ , with the periodogram smoothing being carried out over the entire time domain due to the process stationarity. Thus, as  $\bar{\mathbf{I}}_j^{(Y)}$  is a consistent estimator of  $\beta_j^{(Y)}$  (Park et al., 2014), it follows that it is a consistent estimator of  $\mathbf{S}_j^{(X)}$  and therefore suitable for the optimisation problem (9).

### 3.1.1 Process $\mathbf{Y}$ Simulation

Since we do not have access to the true spectral structure of the original process  $\mathbf{X}$ , we replace it in the above development with its bias-corrected, smoothed estimator  $\{\hat{\mathbf{S}}_j^{(X)}\}_j$  in (4), with the smoothing being taken over the entire time domain due to the process stationarity. In other words, the new process spectral structure is given by

$$\hat{\mathbf{S}}_j^{(Y)} = \sum_{l=1}^J (\mathbf{C}^{-1})_{jl} \hat{\mathbf{S}}_l^{(X)}, \quad \forall j. \quad (10)$$

Due to the desirable properties of the multivariate LSW spectral estimator (Park et al., 2014) and using the continuous mapping theorem (Billingsley, 1999), it follows that  $\hat{\mathbf{S}}_j^{(Y)}$  consistently estimates the target quantity  $\mathbf{S}_j^{(Y)} = \sum_{l=1}^J (\mathbf{C}^{-1})_{jl} \mathbf{S}_l^{(X)}, \forall j$ .

### 3.1.2 Mitigating Sensitivity to the Simulated Realisation of $\mathbf{Y}$

In order to ensure robustness of our proposed procedure to  $\mathbf{Y} = \{\mathbf{Y}_t\}_{t=0}^{T-1}$ , we use a bootstrap-like procedure. Specifically, we simulate  $R$  realisations  $\{\mathbf{Y}^{(r)}\}_{r=1}^R$ , all sharing the spectral structure  $\{\hat{\mathbf{S}}_j^{(X)}\}_j$ , and obtain the associated smoothed periodograms  $\bar{\mathbf{I}}_j^{(\mathbf{Y}^{(r)})}$  at each scale  $j$ , for each replicate  $r = 1, \dots, R$ .

At each scale  $j$ , the average periodogram across the  $R$  replicates,  $\bar{\mathbf{I}}_j = \frac{1}{R} \sum_{r=1}^R \bar{\mathbf{I}}_j^{(\mathbf{Y}^{(r)})}$ , is a consistent estimator of the original spectral structure  $\mathbf{S}_j^{(X)}$ , hence we propose its use in solving (7) and yielding  $\hat{\mathbf{B}}_j^{(Y)}$  as

$$\hat{\mathbf{B}}_j^{(Y)} = \arg \min_{\mathbf{B}_j^{(Y)}} \left\{ -T \left[ \log \det \left( \mathbf{B}_j^{(Y)} \right) - \text{tr} \left( \bar{\mathbf{I}}_j^{(Y)} \mathbf{B}_j^{(Y)} \right) \right] + \mathcal{P} \left( \mathbf{B}_j^{(Y)}, \lambda_j \right) \right\},$$

or equivalently, rewriting it in terms of  $\Theta_j^{(X)}$ ,

$$\hat{\Theta}_j^{(X)} = \arg \min_{\Theta_j^{(X)}} \left\{ -T \left[ \log \det \left( \Theta_j^{(X)} \right) - \text{tr} \left( \bar{\mathbf{I}}_j^{(Y)} \Theta_j^{(X)} \right) \right] + \mathcal{P} \left( \Theta_j^{(X)}, \lambda_j \right) \right\}. \quad (11)$$

**Computational considerations.** (i) The matrix multiplications that yield the input spectral proxy,  $\{\hat{\mathbf{S}}_j^{(X)}\}_j$ , occasionally may result in matrices that are not positively definite. As [Knight et al. \(2024\)](#) document, such issues only occur when using wavelets with short support, e.g. Haar wavelets, and regularisation may be required. In practice, we regularise the estimates using the method of [Schnabel and Eskow \(1999\)](#), as also implemented by [Park et al. \(2014\)](#). (ii) When the observed data is not of dyadic length, we use symmetric padding ([Nason and Silverman, 1994](#)) to achieve a length of the form  $T = 2^J$  for some integer  $J$ .

### 3.1.3 Theoretical Properties

We now establish consistency of the proposed precision estimator obtained via the optimisation problem (9) at a fixed wavelet scale  $j$ . Specifically, we show that the penalised estimator  $\hat{\Theta}_j$  converges in Frobenius norm to the true precision matrix  $\Theta_{0j}$  even when the process dimension,  $P$ , is allowed to grow with the time series length,  $T$ . We hence denote the process dimension by  $P_T$  and assume it to be a non-decreasing function of  $T$ . Theorem 1 below provides an explicit non-asymptotic bound and the resulting convergence rate, under mild assumptions on the underlying Gaussian process and the sparsity of the true graph. We establish the notation below, and make use of the following three assumptions.

**Assumption 1.** The  $P_T$ -dimensional time series  $\mathbf{X} = \{\mathbf{X}_t\}_{t=0}^{T-1}$  is a zero-mean stationary Gaussian process with summable auto- and cross-covariances, namely  $\sum_{\tau=-\infty}^{\infty} |(\mathbf{c}_X(\tau))_{p,q}| < \infty, \forall p, q \in \mathcal{K}$ , where  $\mathbf{c}_X$  denotes the covariance matrix of the process  $\mathbf{X}$ .

**Assumption 2.** Define the set of true edges of the conditional independence graph at a fixed scale  $j$  to be  $\mathcal{E}_{0j} = \{(p, q) \in \mathcal{K} \times \mathcal{K}, p \neq q : (\mathbf{S}_{0j}^{-1})_{p,q} \neq 0\}$ , where  $\mathbf{S}_{0j}$  denotes the true spectrum at scale  $j$ . Denote the true number of edges as  $|\mathcal{E}_{0j}| = E_{0jT}$ , where  $E_{0jT} \ll P_T(P_T - 1)$ , since we are interested in sparse models.

**Assumption 3.** The eigenvalues of  $\Theta_{0j} := \mathbf{S}_{0j}^{-1}$  lie in the interval  $[\phi_{\min}^j, \phi_{\max}^j]$ , where the minimum and maximum eigenvalues satisfy  $0 < \phi_{\min}^j < \phi_{\max}^j < \infty$ , for each scale  $j$ .

Assumption 1 ensures that we have a stationary Gaussian process whose true spectrum,  $\{\mathbf{S}_{0j}\}_j$ , exists. Assumption 2 defines the number of edges in the true graph to be  $E_{0jT}$ , bounded above. Assumption 3 ensures that the true inverse spectrum  $\{\Theta_{0j}\}_j$  exists and its elements are upper-bounded in magnitude.

**Theorem 1.** Let  $P_T$  denote the dimension of the process, allowed to increase with the length of the time series  $T$ , and define

$$r_T = P_T \sqrt{\frac{\log(P_T)}{T}}.$$

Suppose Assumptions 1-3 hold and assume that  $r_T = o(1)$ . Then, the penalised estimator  $\hat{\Theta}_j$  which solves the optimisation problem (9) for  $\Theta_{0j}$  at a fixed wavelet scale  $j$  is such that, for  $\nu > 2$ , there exist constants  $C_0^j, C_1^j, c_1^j > 0$  and for any  $R^j > (C_0^j + C_1^j)/c_1^j$  we have

$$\|\hat{\Theta}_j - \Theta_{0j}\|_F = \mathcal{O}_p(R^j r_T)$$

with probability greater than  $(1 - 1/P_T^{\nu-2})$ , for a fixed scale  $j$ , where  $R^j r_T \rightarrow 0$  as  $T \rightarrow \infty$ . The constants satisfy the conditions below

$$\begin{aligned} C_0^j &= 40 \left( \max_p (\mathbf{S}_{0j})_{p,p} \right) \sqrt{\frac{N_1}{\log(P_T)}}, \text{ where } N_1 = 2 \log(4P_T^{\nu}), \\ c_1^j &= \frac{(\tilde{\phi}_{\max}^j)^{-2}}{2} = \frac{(\phi_{\max}^j + \eta)^{-2}}{2}, \text{ for some } \eta > 0, \text{ and} \\ \lambda'_j &= \frac{\lambda_j}{T} \leq C_1^j \sqrt{\frac{\log(P_T)}{T}}, \text{ for some constant } C_1^j > 0. \end{aligned}$$

The proof of Theorem 1 appears in Appendix A.2, and is heavily reliant on four lemmas, introduced therein.

### 3.2 Model Selection

We now focus on the tuning parameter  $\lambda_j$  of the penalty term in (9) and (11). For the sake of simplicity, we drop the precision matrix process superscript, that is we refer to  $\Theta_j^{(X)}$  as  $\Theta_j$ .

We select the parameter  $\lambda_j$  by minimizing a selection criterion. We present below the information criteria, namely the AIC, BIC, and eBIC, defined as follows,

$$\text{AIC}_j(\lambda) = -2\mathcal{L}(\Theta_j) + 2E_j^*, \quad (12)$$

$$\text{BIC}_j(\lambda) = -2\mathcal{L}(\Theta_j) + \log(T)E_j^*, \quad (13)$$

$$\text{eBIC}_j(\lambda) = -2\mathcal{L}(\Theta_j) + \log(T)E_j^* + 4\gamma \log(P)E_j^*, \quad (14)$$

where  $T$  is the length of the time series,  $E_j^* = TE_j$  and  $E_j$  is the number of non-zero elements in  $\Theta_j$ , and  $\gamma \in [0, 1]$  is the hyperparameter of eBIC. Since our optimisation problem in (9) is defined separately for each scale  $j$ , the information criteria above are scale-dependent too, and the tuning parameter  $\lambda$  will also vary with the scale  $j$ . Also note that (12)–(14) are defined in terms of  $E_j^*$  rather than  $E_j$  due to the approximation error introduced by the discrete wavelet decomposition of continuous processes. As noted by Abramovich et al. (2000), wavelet coefficients are associated with an approximation error of order  $1/\sqrt{T}$ . Since the wavelet-based optimisation (9) is based on the periodogram, which itself has an approximation error of order  $1/T$  (Nason, 2013), we scale  $E_j$  by  $T$  to appropriately account for this discrepancy.

In practice, we use the eBIC criterion and for each scale  $j$ , we restrict the search for  $\lambda$  to a range  $(\lambda_l, \lambda_u)$ , following a similar approach to that in Tugnait (2022). First, we compute  $\lambda_{sm}$ , defined as the smallest value of  $\lambda$  for which the estimated network contains no edges, i.e.,  $\hat{\Theta}_j$  is a diagonal matrix. We then set  $\lambda_u = \lambda_{sm}/3$  and  $\lambda_l = \lambda_u/10$ . This choice of  $\lambda$  values is dependent to the scale representation of the observed process, and excludes both extremely dense and extremely sparse graphs, allowing us to focus the search on a scale-specific range that yields more interpretable and practically relevant models.

### 3.3 Proposed Method for $\mathcal{CIG}$ Estimation: WavTSglasso

Using our proposed method in Section 3.1, we obtain a consistent estimated precision matrix  $\hat{\Theta}_j$  at each scale  $j = 1, \dots, J$ . While the Fourier-based approach calls for an aggregation mechanism over the frequencies (Section 2.1), in our approach we need to aggregate over

scale in order to estimate the  $\mathcal{CIG}$  of the process  $\mathbf{X}$ , or equivalently, an adjacency matrix  $\hat{\mathbf{G}}$ . From Proposition 1, the scale-dependent conditional independence graphs coincide across all scales and this condition will form the basis to our proposal to aggregate the estimated precision matrices across scales, following the strategy introduced next.

We propose to use the following *similarity measure* for each pair of scales  $j$  and  $j'$ ,

$$\Delta(j, j') = \sum_{p=1}^P \sum_{q \neq p} \mathbb{1}\{(\Theta_j)_{p,q} \neq 0, (\Theta_{j'})_{p,q} \neq 0\}, \quad (15)$$

from which we can compute the *scaled similarity measure*

$$\Delta_S(j, j') = \frac{\Delta(j, j')}{\sqrt{E_j} \sqrt{E_{j'}}}. \quad (16)$$

The similarity measure in equation (15) calculates the number of common predicted edges in scales  $j$  and  $j'$ , or put simply, it identifies the common dependencies across scales. Equation (16) then scales  $\Delta(j, j')$  by the number of edges corresponding to each of the scales  $j$  and  $j'$  individually, so that  $\Delta_S(j, j') = 1$  if two the scales  $j$  and  $j'$  yield exactly the same edge(s). We compute  $\Delta_S(j, j')$  for every pair  $(j, j')$  and choose the scale pair  $(j_1, j_2)$  which maximises  $\Delta_S(j, j')$ . If there are no edges in either of the scales, then  $\Delta(j, j') = 0$ , and thus  $\Delta_S(j, j') = 0$ .

Our proposal for the estimation of the conditional graph dependencies is to *combine the estimated precision matrices corresponding to the pair of scales with highest scaled similarity*,  $\hat{\Theta}_{j_1}$  and  $\hat{\Theta}_{j_2}$ , in order to construct the estimated  $\mathcal{CIG}$  adjacency,  $\hat{\mathbf{G}}$ . Specifically, we define  $\hat{\mathbf{G}}_{p,q} = 1$  if  $(\hat{\Theta}_{j_1})_{p,q} \neq 0$  or  $(\hat{\Theta}_{j_2})_{p,q} \neq 0$ , and 0 otherwise. This approach aims to balance the trade-off between sparsity and accuracy. Indeed, when computing the similarity, we focus on edges that are commonly predicted across scales, while the final adjacency incorporates all edges identified at either of the selected scales.

Our proposed  $\mathcal{CIG}$  estimation method, to which we refer as `WavTSglasso`, is summarised in Algorithm 1.

**Proposition 2.** *Under the assumptions of Theorem 1, the estimator  $\hat{\mathbf{G}}$  obtained through the WavTSglasso Algorithm 1 is consistent for the unknown  $\mathcal{CIG}$  adjacency structure,  $\mathbf{G}$ .*

The proof appears in Appendix A.3 and relies on the equivalence of the conditional independence graph structures across scales, as shown in Proposition 1 and the consistency of the scale-based precision estimators established in Theorem 1.

**Similarity measures using more scales.** While we propose to compare two scales at a time, equations (15) and (16) can be easily extended to include more scales if necessary. For example, the corresponding similarity measure formulae with three scales are

$$\begin{aligned} \Delta(j, j', j'') &= \sum_{p=1}^P \sum_{q \neq p} \mathbb{1}\{(\Theta_j)_{p,q} \neq 0, (\Theta_{j'})_{p,q} \neq 0, (\Theta_{j''})_{p,q} \neq 0\}, \\ \Delta_S(j, j', j'') &= \frac{\Delta(j, j', j'')}{\sqrt[3]{E_j} \sqrt[3]{E_{j'}} \sqrt[3]{E_{j''}}}. \end{aligned}$$

Note that in practice, we suggest not to include the coarsest scale when obtaining  $(j_1, j_2)$ , as this would correspond to noisier and less informative spectral estimates.

---

**Algorithm 1:** WavTSglasso

---

**Input:**  $\mathbf{x} = \{\mathbf{x}_t\}_{t=0}^{T-1}$ , a sample of the time series  $\mathbf{X}$  of length  $T = 2^J$  for some  $J \in \mathbb{N}$ ;  
 $R$ , a number of bootstrap replicates.

**Output:**  $\hat{\mathbf{G}}$ , the estimated  $\mathcal{CIG}$  adjacency.

Get  $\{\hat{\mathbf{S}}_j^{(X)}\}_j$  as in (4) smoothed over the entire time-domain.

Compute  $\{\hat{\mathbf{S}}_j^{(Y)}\}_j$  as in (10).

**for**  $r = 1, \dots, R$  **do**

    Simulate  $\mathbf{y}^{(r)}$  with  $\{\hat{\mathbf{S}}_j^{(Y)}\}_j$ .

    Compute smoothed periodogram  $\{\bar{\mathbf{I}}_j^{(\mathbf{Y}^{(r)})}\}_j$ .

    Compute the average periodogram  $\bar{\mathbf{I}}_j^{(Y)}$  at each scale  $j$ .

**for**  $j = 1, \dots, J$  **do**

        Determine a candidate interval  $(\lambda_l, \lambda_u)$  for  $\lambda_j$ .

        Select  $\lambda_j \in (\lambda_l, \lambda_u)$  by minimising the chosen information criterion.

        Compute  $\hat{\Theta}_j$  via (11).

    Obtain  $(j_1, j_2) = \arg \max_{(j, j')} \hat{\Delta}_S(j, j')$ .

    Form  $\hat{\mathbf{G}}$  by combining  $\hat{\Theta}_{j_1}$  and  $\hat{\Theta}_{j_2}$ .

---

## 4 Simulation Study

In this section, we present the results from several simulation studies conducted to evaluate the performance of our proposed WavTSglasso methodology under different scenarios. In particular, we assess how the process dimension  $P$ , the length of the time series  $T$ , and the variability in the sparsity levels (the number of edges relative to their potential total, i.e.,  $s := |\mathcal{E}|/\binom{P}{2}$ ) and in the connection intensities affect  $\mathcal{CIG}$  estimation.

As performance metrics, we compute the following edge detection rates: true positive rate (TPR), false positive rate (FPR), and true discovery rate (TDR) based on the estimated adjacency matrix  $\hat{\mathbf{G}}$  compared to the true adjacency matrix  $\mathbf{G}$  for the conditional independence graph. Let TP and FP denote the number of true positives and false positives, respectively, and let TN and FN denote the number of true negatives and false negatives. Then,

$$\text{TPR} = \frac{\text{TP}}{\text{TP} + \text{FN}}, \quad \text{FPR} = \frac{\text{FP}}{\text{FP} + \text{TN}}, \quad \text{TDR} = \frac{\text{TP}}{\text{TP} + \text{FP}}.$$

We compare our proposed wavelet-based TSglasso algorithm with Fourier-based TSglasso methods, with either  $\ell_1$  or  $\ell_2$  penalisation. All methods are implemented in **R** (R Core Team, 2024). We use the **glasso** package (Friedman et al., 2019) to solve the optimisation problem (11) with  $R = 50$  simulated realisations of  $\mathbf{Y}$ , yielding sparse estimates of the wavelet precision matrix  $\Theta_j$  at each scale  $j$  via a block coordinate descent algorithm. For the Fourier- $\ell_1$  approach, we implement the ADMM algorithm to optimise (2), as proposed by Jung et al. (2015). In addition, we exploit separability of (2) and solve it at each frequency via the **glasso** package. For the Fourier- $\ell_2$  approach, we adopt the ADMM implementation in the **tsglasso** package by Dallakyan et al. (2022). Although their method is a two-stage procedure for sparse VAR estimation, its first stage estimates the precision matrix function using likelihood (2) with an  $\ell_2$ -penalty.

**Data Generating Processes.** Each simulation study comprises  $K = 50$  replicates of a stationary process with known  $\mathcal{CIG}$ , broadly pertaining to a vector autoregressive structure.

First, we generate data based on 10- and 25-dimensional graphs with varying sparsity levels (Section 4.1) and on ring graphs (Section 4.2). These processes are simulated using the generalised network autoregressive (GNAR) model (Knight et al., 2020; Leeming et al., 2024), a multivariate autoregressive process whose univariate series are associated with the nodes of a given graph,  $\mathcal{N}$ . We use the  $r$ -stage neighbour definition of Knight et al. (2020) which establishes nodes  $i$  and  $j$  as  $r$ -stage neighbours if and only if the shortest path between them comprises  $r$  edges of  $\mathcal{E}^{\mathcal{N}}$ . Then, in the GNAR framework, each nodal time series depends on its own past and on the past of its neighbours. Specifically, a  $P$ -dimensional zero-mean Gaussian process  $\mathbf{X}$  is GNAR( $p, [\mathbf{s}]$ ) on the given  $\mathcal{N}$  if

$$\mathbf{X}_t = \sum_{l=1}^p \mathbf{A}_l \mathbf{X}_{t-l} + \boldsymbol{\varepsilon}_t,$$

where

$$\mathbf{A}_l = \text{diag}(\alpha_{l,1}, \dots, \alpha_{l,P}) + \sum_{r=1}^{s_l} \beta_{l,r} \mathbf{W}^{(r)},$$

and  $\mathbf{W}^{(r)}$  denotes the (weighted) neighbour structure at stage  $r$ . Here,  $p \in \mathbb{N}$  is the maximal autoregressive lag,  $[\mathbf{s}] = (s_1, \dots, s_p)$  with  $s_l \in \mathbb{N}$  the maximal stage dependence at lag  $l$ ,  $\alpha_{l,i}$  is the  $i$ -th nodal autoregressive coefficients at lag  $l$ , and  $\beta_{l,r}$  is the network autoregressive coefficient for the  $r$ -th stage neighbour at the  $l$ -th lag.

A subtle but important point to make here is that the given network structure  $\mathcal{N}$  differs from the conditional independence graph  $\mathcal{CIG}$ . As noted by Nason et al. (2025), inter-variable relationships depend on nodes up to twice the largest stage dependence. For example, in a GNAR(1,[1]) model, the adjacency matrix  $\mathbf{G}$  includes both first- and second-stage neighbours in  $\mathcal{N}$ . The numerical experiments in Section 4.1 and 4.2 concern the estimation of the  $\mathcal{CIG}$ , while we postpone the recovery of the underlying graph  $\mathcal{N}$  in GNAR models to Section 5.

In addition to the GNAR models, Section 4.3 considers a vector autoregressive (VAR) and a vector autoregressive moving-average (VARMA) example. For completeness, Table B.1 (Appendix B.1) reports the sparsity level of the  $\mathcal{CIG}$  for each simulated model in Sections 4.1–4.3. Finally, we conclude our discussion with an empirical evaluation in Section 4.4 of our proposed wavelet-based method when varying the number of bootstrap samples of  $\mathbf{Y}$ ,  $R$ .

## 4.1 Effect of Graph Sparsity

We start by investigating how changes in the level of edge sparsity affect the  $\mathcal{CIG}$  estimation. To do this, we simulate data of lengths  $T = 256, 1024$  or  $2048$  from a GNAR(1,[1]) model with  $\beta_{1,1} = 0.85$  over 10-dimensional graphs. These graphs are constructed by forming edges between pairs of nodes with a given probability  $\rho \in [0, 1]$  for each possible pair, known as Erdős–Rényi (ER) graphs (Erdős and Rényi, 1959). By varying the value of  $\rho$ , we generate graphs with different levels of sparsity. Specifically, we create two random 10-dimensional ER graphs with  $\rho = 0.1, 0.4$ , as shown in Figure 2, and note our methodology allows graph topologies with disconnected nodes.

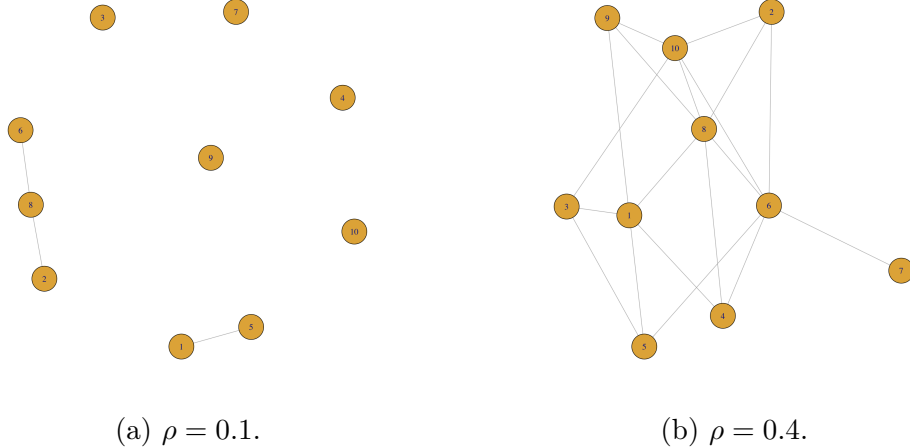


Figure 2: Two 10-dimensional Erdős-Renyi graphs with varying levels of sparsity, corresponding to different values of the connection probability  $\rho$ , as described in the text.

We estimate the conditional dependence structure using our proposed wavelet-based method and benchmark it against three Fourier-based methods: Fourier- $\ell_1$  with either glasso or ADMM, and Fourier- $\ell_2$  with the ADMM approach. The corresponding edge detection rates over the  $K = 50$  series realisations for all methods with  $T = 1024$  are reported in Table 1 below and analogous results for  $T = 256$  and  $T = 2048$  are shown in Tables B.2 and B.3 (Appendix B.2).

Overall, our proposed `WavTSGlasso` estimation procedure outperforms the other methods, achieving higher TPR and TDR values and lower FPR values. When comparing edge rates across different time lengths, the wavelet-based approach remains quite stable, with edge rates consistently within the same magnitude for sparser graphs. The method appears less robust in the denser cases ( $\rho = 0.4$ ), but this is also observed for the Fourier- $\ell_1$  methods, and shows smaller variability than the Fourier methods with changes in  $T$ .

Similarly, our wavelet-based glasso strategy remains relatively stable across different levels of network sparsity. However, its performance tends to degrade as the graph becomes more connected. Specifically, the TPR tends to decrease and the FPR increases. This trend is also observed in the Fourier- $\ell_1$  methods, which often exhibit higher FPR than the wavelet-based method. On the other hand, the Fourier- $\ell_2$  approach shows higher TPR values for the denser network, but this comes at the cost of significantly higher FPR values. This suggests that the Fourier-based method tends to produce overly dense network estimates. Overall, the proposed wavelet-based approach is the preferred choice, producing the best discovery results across most scenarios. Plots of the average estimated adjacency matrices are provided in Figures B.2–B.3 in Appendix B.3.

	$\rho = 0.1$			$\rho = 0.4$		
	TPR	FPR	TDR	TPR	FPR	TDR
W - $\ell_1$	<b>0.9950</b>	<b>0.0057</b>	<b>0.9648</b>	<b>0.8812</b>	<b>0.1300</b>	<b>0.9735</b>
F - $\ell_1$ (glasso)	1	0.0996	0.4888	0.8029	0.1650	0.9631
F - $\ell_1$ (ADMM)	1	0.2096	0.3152	0.8195	0.1550	0.9960
F - $\ell_2$ (ADMM)	1	0.0187	0.8510	0.9205	0.3175	0.9406

Table 1: True Positive, False Positive and True Discovery Rates for 10-dimensional GNAR(1,[1]) models over Erdős-Renyi graphs for  $T = 1024$ . Values in bold identify the best method overall, considering aggregated TPR, FPR, and TDR values.

In addition to this standard setup, we examine the robustness of our methodology when the time series data are generated from different GNAR models. Specifically, we generate processes of length  $T = 1024$  from a GNAR(2,[1,1]) process with parameters  $\beta_{1,1} = \beta_{2,1} = 0.4$ . Similarly, we analyse the GNAR(1,[2]) model with  $\beta_{1,1} = \beta_{1,2} = 0.4$  and  $T = 1024$ , simulated over two random 25-dimensional ER graphs with  $\rho = 0.05, 0.1$  (see Figure 3). We choose a higher-dimensional graph in this case to maintain sparsity in the conditional-dependence structure, given the increased neighbour-stage dependence.

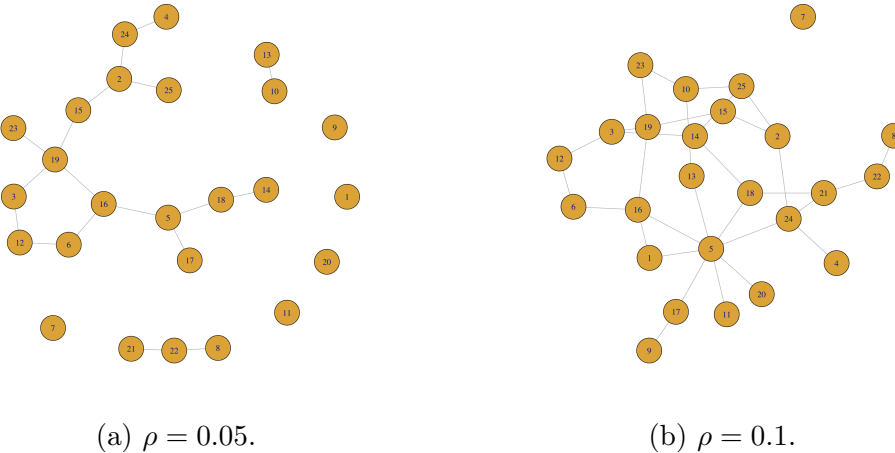


Figure 3: Two 25-dimensional Erdős-Renyi models with varying levels of sparsity.

In Appendix B.2, Table B.4 shows the edge detection rates for the 10-dimensional GNAR(2,[1,1]) models. The wavelet-based approach provides excellent graph discovery across both sparsity levels when compared to the other methods. Even in the sparsest case, when  $\rho = 0.1$ , although the  $\ell_2$ -based Fourier method yields the best overall performance, the wavelet method achieves very similar edge rates, with only a slightly higher FPR.

On the other hand, Table B.5 reports the performance measures for the GNAR(1,[2]) models. Once again, the proposed wavelet approach is competitive in recovering the graph's

dependence structure. The corresponding average adjacency matrices for these experiments are shown in Figures B.4–B.7 in Appendix B.3.

## 4.2 Effect of Strength of Neighbourhood Dependence

We now investigate the accuracy of the estimation methods when the dependence on the neighbours in the graph varies. In the GNAR framework, this is encoded in the network parameter  $\beta$ , where a high  $\beta$ -value (close to 1) refers to a strong connection between neighbours and low  $\beta$ -value (close to 0) refers to a weak connection. In these experiments, we simulate processes of length  $T = 1024$  from a GNAR(1,[1]) model over either a 10- or 25-dimensional Ring, as displayed in Figure 4.

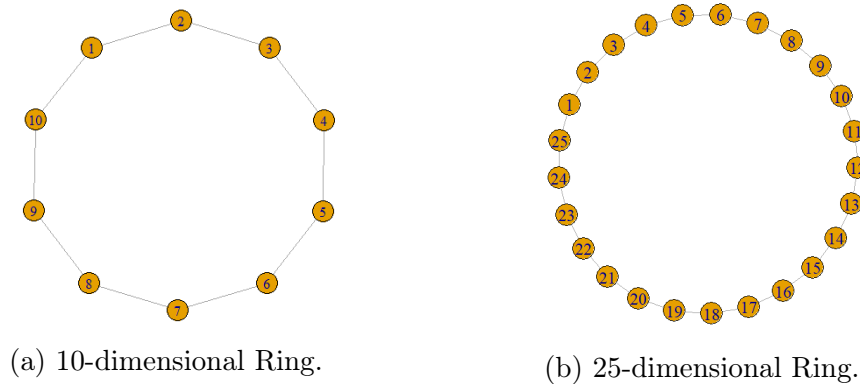


Figure 4: Network structure for 10 and 25 dimensional rings.

Tables 2 (below) and B.6 (Appendix B.2) report the average edge rates of the wavelet approach based on  $K = 50$  replicates, comparing results to the Fourier methods for the 10-dimensional ring and 25-dimensional ring respectively. We generate realisations from two models corresponding to  $\beta_{1,1} = 0.65, 0.35$  and the two differently sized ring graphs, and the best results for each model are highlighted in bold. In particular, our proposed wavelet-based method proposed in Section 3 outperforms all Fourier-based methods for both the 10- and 25-dimensional ring structures.

Furthermore, we note that the TDR becomes more sensitive to false positives when moving from the 10-dimensional ring to the 25-dimensional ring – the number of possible false positives increases from 35 to 275. As a result, even if the FPR remains roughly constant, the absolute number of false positives is substantially higher, leading to a decrease in the TDR.

Appendix B.4 shows the average estimated adjacency matrices for the 10-dimensional (Figures B.8–B.9) and the 25-dimensional (Figures B.10–B.11) models.

	$\beta = 0.65$			$\beta = 0.35$		
	TPR	FPR	TDR	TPR	FPR	TDR
W - $\ell_1$	<b>0.7472</b>	<b>0.0409</b>	<b>0.7877</b>	<b>0.4940</b>	<b>0.0964</b>	<b>0.5460</b>
F - $\ell_1$ (glasso)	0.6943	0.0643	0.6765	0.0080	0	1
F - $\ell_1$ (ADMM)	0.4284	0	1	0.0688	0.0002	0.9943
F - $\ell_2$ (ADMM)	0.6196	0.0176	0.8798	0.7952	0.4966	0.2529

Table 2: True Positive, False Positive and True Discovery Rates for 25-dimensional GNAR(1,[1]) ring models for  $T = 1024$ . Values in bold identify the best method overall, considering aggregated TPR, FPR, and TDR values.

### 4.3 VAR and VARMA Models

In the previous sections, we evaluated our proposed `WavTSglasso` technique on data simulated from models with a common cross-nodal dependence parameter  $\beta$  across all connections. Here, we examine how variability in the connections affects recovery of  $\mathbf{G}$ . To this end, we consider a 10-dimensional VAR(1) processes,  $\mathbf{X}_t = \mathbf{A}\mathbf{X}_{t-1} + \boldsymbol{\varepsilon}_t$ , where  $\mathbf{A} = (A_{i,j}) \in \mathbb{R}^{10 \times 10}$  is the coefficient matrix and  $\{\boldsymbol{\varepsilon}_t\}_t$  is a zero-mean Gaussian noise process with  $\boldsymbol{\Sigma}_\varepsilon = \mathbf{I}_{10}$  for all  $t$ . Define

$$\mathbf{A} = \begin{pmatrix} 0 & \beta_1 & 0 & \cdots & \cdots & \cdots & \beta_1 \\ \beta_2 & 0 & \beta_2 & 0 & \cdots & \cdots & 0 \\ 0 & \beta_3 & 0 & \beta_3 & \cdots & \cdots & 0 \\ \vdots & \vdots & \ddots & \ddots & \ddots & \ddots & \vdots \\ 0 & \cdots & \cdots & \beta_9 & 0 & \beta_9 & \\ \beta_{10} & 0 & \cdots & 0 & \beta_{10} & 0 & \end{pmatrix}, \quad (17)$$

so that variability in the coefficient matrix is introduced via the coefficients  $\{\beta_i\}_{i=1}^{10}$ . Specifically, we consider two intervals of differing widths, namely  $I_1 = (0.6, 0.7)$ ,  $I_2 = (0.4, 0.9)$ , and we randomly draw  $\beta_i$ ,  $i = 1, \dots, 10$ , from each interval in turn. The dependence graph of these two VAR(1) processes matches the 10-dimensional GNAR(1,[1]) models with Ring graph of Section 4.2. In particular, the special case  $\beta_i = \beta_{1,1}$  for all  $i = 1, \dots, 10$  coincides with the GNAR(1,[1]) Ring model with network parameter  $\beta_{1,1}$ .

All simulation studies used  $K = 50$  realisations of length  $T = 1024$ , and we fix  $R = 50$  bootstrap samples for our wavelet- $\ell_1$  method. As shown by the edge detection rate results in Table B.7 (Appendix B.2), performance gets worse for all four approaches as variability in  $\mathbf{A}$  increases, but the wavelet method still performs better than the Fourier-based approaches. In particular, the FPRs of the wavelet estimates remain relatively stable across the four simulations, while the TPR decreases as variability grows, indicating sparser estimated adjacency matrices. Even so, the wavelet-based estimates remain reasonable compared with the Fourier counterparts, which tend to be either sparser (Fourier- $\ell_1$  and Fourier- $\ell_2$  with ADMM algorithm) or denser but with higher FPR (Fourier- $\ell_1$  with glasso algorithm).

We also consider the case when the dependence graph is not determined by the coefficient

matrix  $\mathbf{A}$ . Similar to [Fiecas et al. \(2019\)](#), we construct a 10-dimensional VAR(1) process in which the true sparse structure of  $\mathbf{G}$  matches that of the precision matrix of the noise process. This is achieved by using a diagonal coefficient matrix, here we set  $\mathbf{A} = 0.5 \mathbf{I}_{10}$ . Then, the off-diagonal entries of  $\Sigma_{\epsilon}^{-1}$  are randomly set to 0 or 0.5 with probability 0.5, and the diagonal entries are adjusted to ensure positive definiteness.

Further, we also consider the 20-dimensional VARMA(2,2) model in [Wilms et al. \(2023\)](#)

$$\mathbf{X}_t = \mathbf{A}_1 \mathbf{X}_{t-1} + \mathbf{A}_2 \mathbf{X}_{t-2} + \boldsymbol{\epsilon}_t + \mathbf{B}_1 \boldsymbol{\epsilon}_{t-1} + \mathbf{B}_2 \boldsymbol{\epsilon}_{t-2}, \quad (18)$$

where  $\{\boldsymbol{\epsilon}_t\}_t$  is a zero-mean Gaussian noise process with identity covariance matrix. The autoregressive coefficient matrices are diagonal:  $\mathbf{A}_1 = 0.4 \mathbf{I}_{20}$  and  $\mathbf{A}_2 = 0.2 \mathbf{I}_{20}$ . The moving-average matrices are block-diagonal, with  $5 \times 5$ -dimensional blocks  $1.5(\mathbf{I}_5 + \mathbf{J}_5)$  for  $\mathbf{B}_1$ , and  $0.75(\mathbf{I}_5 + \mathbf{J}_5)$  for  $\mathbf{B}_2$ , where  $\mathbf{J}_5$  denotes the  $5 \times 5$ -dimensional matrix whose entries are all 1. Consequently, the dependence graph of (18) inherits this block-diagonal structure.

Table 3 reports the estimation performance of the four methods on data of length  $T = 1024$ . The proposed wavelet-based method outperforms all Fourier approaches when taking all detection rates into consideration, albeit it produces a higher FPR. In particular, it appears the adjacency matrix  $\mathbf{G}$  induced by the VAR(1) process is difficult to recover, and both Fourier- $\ell_1$  methods fail to estimate it accurately. For the VARMA model (18), our proposed `WavTSGlasso` recovers the adjacency perfectly, whereas the Fourier methods perform poorly due to high FPRs. Inspecting the aggregated recovery heatmaps in Figure B.15 in Appendix B.5, the block-diagonal structure is still discernible in the Fourier-based estimates. However, those methods do not shrink small off-diagonal entries of the inverse spectral density matrix exactly to zero, while our wavelet method does so successfully.

	VAR(1) Model			VARMA(2,2) Model		
	TPR	FPR	TDR	TPR	FPR	TDR
W - $\ell_1$	<b>0.7909</b>	<b>0.2493</b>	<b>0.7199</b>	<b>1</b>	<b>0</b>	<b>1</b>
F - $\ell_1$ (glasso)	0.0018	0	1	1	0.8678	0.2242
F - $\ell_1$ (ADMM)	0.0609	0.0257	0.7217	1	0.5508	0.3132
F - $\ell_2$ (ADMM)	0.3964	0.2300	0.6235	1	0.9368	0.2107

Table 3: True Positive, False Positive and True Discovery Rates for the VAR and VARMA models whose dependence graph are not determined by the autoregressive component. Values in bold identify the best method overall, considering aggregated TPR, FPR, and TDR values.

#### 4.4 Empirical Evaluation of Bootstrapping

We now empirically assess the performance of our proposed technique when using different numbers of bootstrap samples  $R$ . We also compare our `WavTSGlasso` method with the corrected spectral estimator in equation (4) in place of the averaged periodogram  $\{\bar{\mathbf{I}}_j^{(Y)}\}_j$  employed in the optimisation problem (11) in order to compare our proposed `WavTSGlasso` with the optimisation problem as proposed by [Gibberd and Nelson \(2015b\)](#) in equation (5).

However, note that our implementation differs from their proposal in two key aspects – firstly, prior to correction, the periodogram smoothing is taking place over the entire time domain, and secondly, and most importantly, we have used our proposed method for aggregating the scales in order to estimate the final adjacency matrix, a step entirely missing in [Gibberd and Nelson \(2015b\)](#).

Table 4 shows the edge detection rates for the Erdős-Renyi models of Section 4.1 with  $T = 1024$ . Analogous tables with  $T = 256$  and  $T = 2048$  are shown in Tables B.8 and B.9 (Appendix B.2). As expected, increasing the number of bootstrap simulations improves performance, with a noticeable gain already observed when moving from 1 to 10 simulated processes, and a plateau in results beyond  $R = 50$  bootstraps. Moreover, when no bootstrapping is applied, the method’s performance becomes more sensitive to the number of observations  $T$ .

	$\rho = 0.1$			$\rho = 0.4$		
	TPR	FPR	TDR	TPR	FPR	TDR
$R = 1$	0.9700	0.0096	0.9320	0.8052	0.0975	0.9779
$R = 10$	1	0.0078	0.9529	0.8767	0.1150	0.9766
$R = 50$	0.9950	0.0057	0.9648	0.8812	0.1300	0.9735
$R = 100$	0.9950	0.0048	0.9722	0.9029	0.1125	0.9776
$\hat{\mathbf{S}}^{(X)}$	0.9950	0.0009	0.9933	0.9667	0.3600	0.9358

Table 4: True Positive, False Positive and True Discovery Rates for 10-dimensional GNAR(1,[1]) models over Erdős-Renyi graphs for  $T = 1024$  and with different number of bootstrap samples  $R$ ; (last row) `WavTSglasso` with corrected periodogram (4).

Table 5 (below) reports the average TPR, FPR, and TDR across  $K = 50$  replicates for two 25-dimensional GNAR(1,[1]) processes corresponding to  $\beta_{1,1} \in \{0.65, 0.35\}$ , under varying numbers of bootstrap samples,  $R$ . Table B.10 (Appendix B.2) reports results for the 10-dimensional GNAR(1,[1]) process. We observe that stronger connections between neighbouring nodes yield better performance, i.e. the dependence structure is more easily identified—higher TPR and TDR values, and lower FPR values—even with few (or no) bootstrap samples. Likewise, performance improves markedly as the number of bootstraps increases when  $\beta_{1,1}$  is smaller. This is expected, since  $\beta$  encodes the strength of connections among nodes, and additional bootstrap samples lead to better estimation.

When using the `WavTSglasso` method with the bias-corrected spectral estimator  $\{\hat{\mathbf{S}}_j^{(X)}\}_j$ , the results show that it still yields numerically competitive TPR and TDR, although this construction is not directly supported by the likelihood theory underlying our optimisation, as  $\{\hat{\mathbf{S}}_j^{(X)}\}_j$  is only a robust approximation to the true spectral structure. This, however, comes at the cost of higher FPR, especially for denser models or for those with weaker dependencies.

	$\beta = 0.65$			$\beta = 0.35$		
	TPR	FPR	TDR	TPR	FPR	TDR
	$R = 1$	0.4632	0.1087	0.4606	0.3140	0.1925
$R = 10$	0.6556	0.0552	0.7108	0.4740	0.1374	0.4229
$R = 50$	0.7472	0.0409	0.7877	0.4940	0.0964	0.5460
$R = 100$	0.7884	0.0359	0.8224	0.5052	0.0761	0.6060
$\hat{\mathbf{S}}^{(X)}$	0.8952	0.0073	0.9604	0.6344	0.1186	0.5228

Table 5: True Positive, False Positive and True Discovery Rates for 25-dimensional GNAR(1,[1]) ring models with  $T = 1024$  and with different number of bootstrap samples  $R$ ; (last row) `WavTSglasso` with corrected periodogram (4).

## 5 Underlying Graph Discovery

So far, we have focussed on inferring the conditional dependence structure,  $\mathcal{CIG} = (\mathcal{K}, \mathcal{E})$  underlying the observed data. In this section, we focus on finding the underlying network (graph)  $\mathcal{N} = (\mathcal{K}, \mathcal{E}^{\mathcal{N}})$ , when such a network is indeed present in the data, such as for the GNAR models in Section 4. Note that these two tasks are crucially not identical.

If the data follows a GNAR( $p, [\mathbf{s}]$ ) process or, more generally, if we assume the data has an underlying graph structure  $\mathcal{N}$ , then estimating the edge set  $\mathcal{E}^{\mathcal{N}}$  of such a graph is crucial for inference. We denote the adjacency matrix of the underlying graph by  $\mathbf{G}^{\mathcal{N}}$ , and recall we denote the adjacency of the conditional independence graph,  $\mathcal{CIG}$ , by  $\mathbf{G}$ . Since  $\mathcal{E}^{\mathcal{N}}$  is contained within  $\mathcal{E}$  (Nason et al., 2025, Theorem 2), the task is to determine which edges in  $\mathbf{G}$  correspond to those of  $\mathbf{G}^{\mathcal{N}}$ .

From the proposed `WavTSglasso` approach described in Section 3, we obtain the sparse estimated precision matrices  $\hat{\Theta}_j$  for each scale  $j = 1, \dots, J$ , and define the corresponding scale-dependent edge and precision value sets as

$$\begin{aligned}\mathcal{E}_j^{(\mathbf{G})} &= \{(p, q) \in \mathcal{K} \times \mathcal{K}, p \neq q : (\hat{\Theta}_j)_{p,q} \neq 0\}, \\ \vartheta_j^{(\mathbf{G})} &= \{(\hat{\Theta}_j)_{p,q} : (p, q) \in \mathcal{E}_j^{(\mathbf{G})}\}, \text{ respectively.}\end{aligned}$$

We propose applying  $k$ -means clustering to the precision values  $\vartheta_j^{(\mathbf{G})}$  to separate them into  $k = 2$  clusters: those that correspond to edges in  $\mathbf{G}^{\mathcal{N}}$  and the additional edges in  $\mathbf{G}$  (a ‘noise’ cluster). The  $k$ -means clustering procedure yields a cluster,  $\mathcal{C}_{1j}$ , containing edges with low values of  $|(\hat{\Theta}_j)_{p,q}|$ , or in other words, those edges between node pairs  $(p, q)$  that are the least significant; this is the cluster whose centre is closest to 0, hence the ‘noise’ cluster. The second cluster,  $\mathcal{C}_{2j}$ , contains the remaining edges in  $\mathbf{G}$ , thus we let  $(\hat{\mathbf{G}}_j^{\mathcal{N}})_{p,q} = 1$  when  $(p, q) \in \mathcal{C}_{2j}$ , and zero otherwise, in order to obtain a *scale  $j$ -dependent* sparse estimator for the underlying graph adjacency  $\mathbf{G}^{\mathcal{N}}$ .

Our strategy for scale selection in order to yield  $\hat{\mathbf{G}}^{\mathcal{N}}$  is data-dependent. When the underlying network is expected to be sparse and the GNAR neighbourhood structure is

simple (such as a  $\text{GNAR}(1,[1])$  or a  $\text{GNAR}(2,[1,1])$ ), we recommend using the finest scale (scale 1). For denser networks with similarly simple neighbourhood structure or if the neighbourhood structure is more complex (such as a  $\text{GNAR}(1,[2])$ ), then a middle scale ( $j = \lfloor J/2 \rfloor$ ) is recommended.

The effects of dimension, sparsity and length of the time series on the network estimation are assessed in what follows via simulation, akin to our `WavTSglasso` experiments. We compute the TPR, FPR and TDR for each simulation, comparing the estimated adjacency matrix  $\hat{\mathbf{G}}^{\mathcal{N}}$  to the true adjacency matrix  $\mathbf{G}^{\mathcal{N}}$ . Since, to our knowledge, there are no other algorithms which attempt to identify the underlying network,  $\mathcal{N}$ , we only report results using our clustering methodology.

**Use of other clustering techniques.** We choose  $k$ -means for edge-selection due to its simplicity and speed but other clustering algorithms can be used. We have found that experimental results change only minimally when other clustering techniques such as tree-based procedures, (Johnson, 1967) or  $k$ -medoids (Kaufman and Rousseeuw, 1987) are used.

## 5.1 Simulation Results for GNAR Models defined on Erdős-Renyi Graphs

We report results for the Erdős–Renyi (ER) networks introduced in Section 4.1. For the baseline setting, we simulate time series of length  $T \in \{256, 1024, 2048\}$  for a  $\text{GNAR}(1,[1])$  model with  $\beta_{1,1} = 0.85$  over 10-node graphs. Graph density is controlled by the ER edge probability  $\rho \in \{0.1, 0.4\}$ , corresponding to the two networks in Figure 2.

Table 6 reports TPR, FPR, and TDR results illustrating the clustering performance is relatively stable with increasing  $T$  for sparse graphs. As  $\rho$  increases, hence the edge sparsity decreases, stability and overall performance unsurprisingly deteriorate, as consistent with the growing difficulty of recovering the underlying dependence structure.

We study two alternative network dynamics, also introduced in Section 4.1. Firstly, a  $\text{GNAR}(2,[1,1])$  model and  $\beta_{1,1} = \beta_{2,1} = 0.4$  on the same 10-node ER graphs used for the  $\text{GNAR}(1,[1])$  case. Secondly, a  $\text{GNAR}(1,[2])$  model with  $\beta_{1,1} = \beta_{1,2} = 0.4$  on two 25-node ER graphs with  $\rho \in \{0.05, 0.1\}$  as shown in Figure 4. Both models are simulated with  $T = 1024$ . Results corresponding to the  $\text{GNAR}(2,[1,1])$  and the  $\text{GNAR}(1,[2])$  processes appear in Appendix C.2, Tables C.11 and C.12, which closely mirror Table 6. We note the performance degrades as graphs become denser for the  $\text{GNAR}(2,[1,1])$  model as in the  $\text{GNAR}(1,[1])$  model. The clustering procedure finds it harder to disentangle the more complex neighbourhood structure, reducing the network edge-discovery accuracy, as also compounded by the lower accuracy in the estimation of the dependence graph itself, which is demonstrated by the  $\text{GNAR}(1,[2])$  results. The estimated adjacency matrices are reported in Appendix C.2 (Figures C.16–C.21). Since the results of the recovery of  $\mathbf{G}^{\mathcal{N}}$  depend on the results of the recovery of  $\mathbf{G}$ , the trends in  $\hat{\mathbf{G}}^{\mathcal{N}}$  mirror those described in Section 4.1 for the conditional dependence graph,  $\hat{\mathbf{G}}$ .

	$\rho = 0.1$			$\rho = 0.4$		
	TPR	FPR	TDR	TPR	FPR	TDR
$T = 256$	0.9867	0	1	0.5811	0.1039	0.7941
$T = 1024$	1	0	1	0.5989	0.1006	0.7930
$T = 2048$	1	0	1	0.6995	0.1374	0.7618

Table 6: True Positive, False Positive and True Discovery Rates for 10-dimensional GNAR(1,[1]) models over Erdős-Renyi graphs. Results for data with  $T = 256$  are shown in the first row,  $T = 1024$  are in the second row, and  $T = 2048$  are in the third rows.

## 5.2 Simulation Results for GNAR Models defined on Ring Graphs

We now assess how the estimation performance varies as the dependence on the neighbours vary. We can vary the dependence on the neighbours in the GNAR models by varying the network parameter  $\beta$ , with a strong connection depicted by a  $\beta$ -value close to 1 and a weak connection depicted by a  $\beta$  value close to 0. We simulate GNAR(1,[1]) models over a 10- or 25-dimensional ring with length  $T = 1024$ , as shown in Figure 4.

As in Section 4.2, we evaluate two models per ring with  $\beta \in \{0.65, 0.35\}$ . Table 7 reports results for the 10- and 25-node rings. Consistent with the results in Section 4.2, edge-discovery rates decline as the neighbourhood strength weakens in both dimensions, while the ability to identify absent edges remains high across all models. The average estimated adjacency matrices for these experiments can be visualised in Appendix C.3.

	$\beta = 0.65$			$\beta = 0.35$		
	TPR	FPR	TDR	TPR	FPR	TDR
$P = 10$	0.972	0	1	0.696	0.0005	0.9982
$P = 25$	0.7488	0.0001	0.9990	0.5912	0.003	0.9534

Table 7: True Positive, False Positive and True Discovery Rates for 10- and 25-dimensional GNAR(1,[1]) models over Ring graphs with  $T = 1024$ . Results for 10-dimensional Ring are shown in the first row, and 25-dimensional Ring results are shown in the second row.

## 6 Application to COVID-19 Data

We now apply our network estimation methodology to the motivating epidemiology dataset introduced in Section 1. We consider the daily recorded number of COVID-19 patients transferred to mechanical ventilation beds across various NHS Trusts in England, covering the period from April 2020 to July 2021. Specifically, the dataset consists of count data for 140 NHS Trusts, each with  $T = 456$  observations. A logarithmic transformation is applied to stabilise the variance and bring the data closer to normality. The dataset is available in the GNAR package (Leeming et al., 2024) and was first analysed by Nason et al. (2025). Since

the true graph structure of dependencies is unknown, our aim is to estimate and visualise a sparse dependence graph pertaining to the data.

We begin by extending each time series to length  $T = 512$  by symmetric padding to match  $J = 9$  wavelet scales. We apply a stationarity test (Nason, 2013) and retain only those series that satisfy the stationarity assumption. Based on this test, we exclude 52 NHS Trusts. Additionally, we remove 7 trusts whose codes do not appear in the NHS reference spreadsheet, resulting in an observed multivariate process over  $P = 81$  nodes.

As in Nason et al. (2025) who used geographic distance as a basis for defining network structure, we organise the nodes by NHS region to examine how nearby Trusts may influence one another. We group NHS Trusts into regional categories in order to explore how dependency patterns vary geographically from North to South. Specifically, nodes 1–26 correspond to Trusts in the North, nodes 27–47 to the Midlands, and nodes 48–81 to the South. Table D.13 (Appendix D) breaks down the node allocation for each NHS England Region.

**$\mathcal{CIG}$  estimation using the WavTSglasso proposal from Section 3.** Firstly, we estimate and visualise the dependence structure in the data. We apply our proposed wavelet-based method, as described in Algorithm 1, with  $R = 50$  bootstraps as aligned to our simulation study findings. The similarity measure in (16) selects the two finest scales,  $(j_1, j_2) := (1, 2)$ , for the estimation of the adjacency matrix  $\mathbf{G}$ . Upon inspection, these two scales exhibit substantial overlap in estimated edges. The adjacency matrix appears in Figure 5 and has a sparsity level of 68.5% which falls within the range of sparsity levels that were tested in our simulation study, as shown in Table B.1 (Appendix B.1).

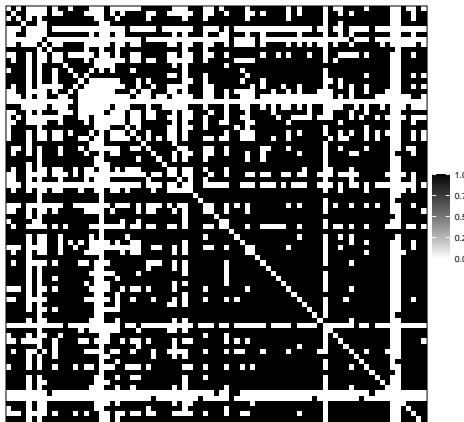
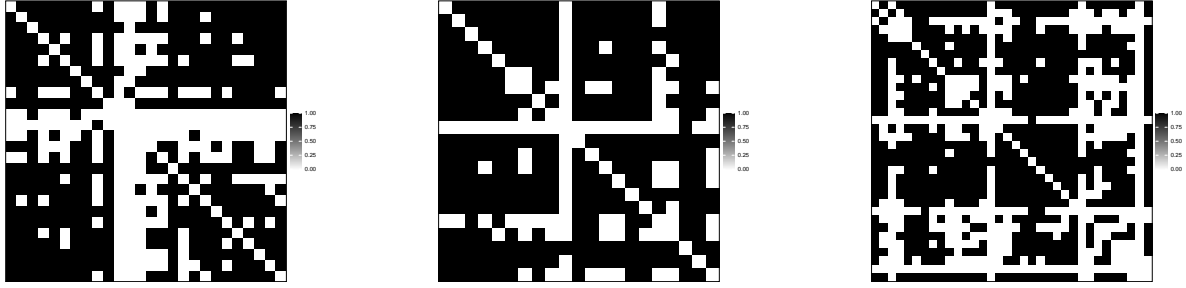


Figure 5: Estimated adjacency matrix for the conditional independence graph using the proposed WavTSglasso method from Section 3 for the COVID-19 ventilation beds dataset. A black square corresponds to a connection between the associated trusts and a white square corresponds to no connection between the associated trusts. The nodes (NHS trusts) are arranged from the North to the South of England.

Figure 6 shows the estimated adjacencies for the North, Midlands and South trusts, thus illustrating the different conditional dependence structures between the NHS England Trusts, specific to their geographical location.

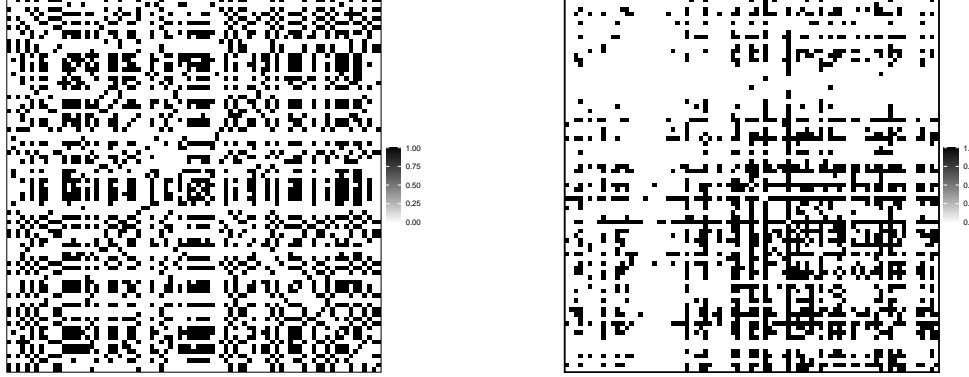


(a) Estimated adjacency for the North of England. (b) Estimated adjacency for the Midlands. (c) Estimated adjacency for the South of England.

Figure 6: Estimated adjacency matrices for the conditional independence graph for the (a) North of England, (b) Midlands, and (c) South of England using the proposed `WavTSglasso`. For each plot, nodes (NHS trusts) are plotted from West to East.

**Network  $\mathcal{N}$  estimation using the strategy proposed in Section 5.** We now consider the estimation of the underlying network for GNAR modelling using the clustering method described in Section 5. [Nason et al. \(2025\)](#) show that the data can be appropriately modelled by a GNAR(1,[1]) model, and in-line with our previous findings we use the finest scale ( $j = 1$ ) to cluster the edges of the estimated  $\mathcal{CIG}$  adjacency matrix,  $\hat{\mathbf{G}}$ . This is since the model order is low and the network sparsity falls between 0.1 and 0.4, as investigated in our simulation section (see Table B.1). The right panel of Figure 7 shows the estimated adjacency matrix of the underlying network,  $\hat{\mathbf{G}}^{\mathcal{N}}$ , using the clustering method from Section 5. The adjacency of the network used by [Nason et al. \(2025\)](#), available in the GNAR R package ([Leeming et al., 2024](#)), is illustrated in the left panel of Figure 7. Recall that [Nason et al. \(2025\)](#) employ a user-defined distance-metric to obtain the network, namely by connecting any two trusts which are within 120km of each other. However, this forms a more densely connected network in comparison to the data-driven network estimated using our clustering method.

Similarly, the right panels of Figure 8 show the estimated network at a regional level (corresponding to the regional  $\mathcal{CIG}$  Figures 6a–6c), together with the network used by [Nason et al. \(2025\)](#) in those regions in the left panels. Note the estimated adjacency for the Midlands (middle row) is more densely populated than its counterparts for the South (bottom row) or for the North (top row). This could be due to the Midlands being geographically central and therefore well-connected to both the North and South of England and hence there may be more connections in the Midlands in the underlying network.



(a) Adjacency used in [Nason et al. \(2025\)](#). (b) Estimated adjacency using clustering method.

Figure 7: Estimated adjacency matrix for the underlying graph associated to the COVID-19 ventilation beds dataset where a black square corresponds to a connection between the associated trusts and a white square corresponds to no connection between the associated trusts. Figure (a) shows the adjacency used in [Nason et al. \(2025\)](#); (b) shows the estimated adjacency using the clustering method from Section 5.

**Benefit of data-driven network estimation for forecasting.** Let us now evaluate our data-inferred network versus a user-based construction, in the context of prediction – one of the key targets in [Nason et al. \(2025\)](#), although not a task in itself for our development here. Table 8 reports multi-step-ahead mean squared prediction errors (MSPEs) for forecasts based on the adjacency matrix proposed by [Nason et al. \(2025\)](#) (Figure 7a) and on the WavTSglasso-derived network (Figure 7b), where we adopted a GNAR(1,[1]) model as proposed by [Nason et al. \(2025\)](#). For nodes with no neighbours in the estimated network, the GNAR(1,[1]) specification naturally reduces to a univariate AR(1) forecasting model. Across all horizons from one to five steps ahead the WavTSglasso-derived network delivers slightly lower MSPEs than the network used in [Nason et al. \(2025\)](#), indicating an improved predictive performance with reductions in MSPE ranging from 2% to 12% when using our discovered network, with the most significant improvements at medium horizons. These results suggest that the wavelet-based inferred network captures epidemiologically relevant connectivity that is not fully represented by the hand-tuned distance-based approach used by [Nason et al. \(2025\)](#).

Step ahead	MSPE ( <a href="#">Nason et al. (2025)</a> )	MSPE ( <a href="#">WavTSglasso</a> )
1	0.0305	0.0300
2	0.0377	0.0344
3	0.0740	0.0681
4	0.1220	0.1104
5	0.1263	0.1122

Table 8: Mean Squared Prediction Error comparisons for one to five step ahead forecasts from a GNAR(1,[1]) model using the network suggested by [Nason et al. \(2025\)](#) (seen in Figure 7a) and the network suggested by our wavelet-based approach (seen in Figure 7b).

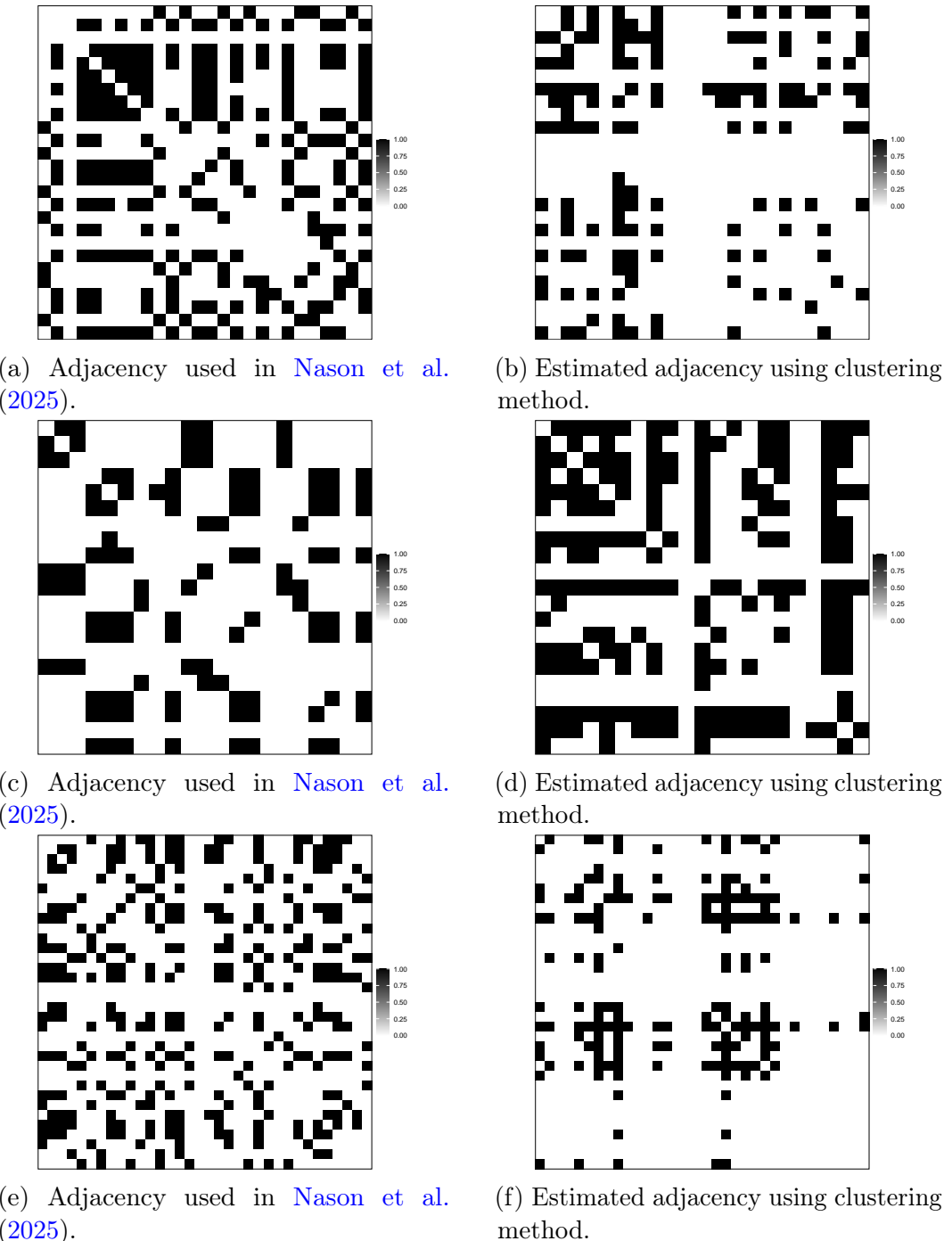


Figure 8: Underlying network adjacency matrices for the COVID-19 ventilation beds data. Rows depict: North (top), Midlands (middle), South (bottom) associated NHS trusts. Columns depict: adjacency used in Nason et al. (2025) (left); estimated adjacency using the clustering method from Section 5 (right).

## 7 Conclusions and Further Work

In this article, we proposed a novel wavelet domain method for estimating the conditional independence graph ( $\mathcal{CIG}$ ) of second-order stationary time series. By considering the distributional properties of the wavelet coefficients associated to the process, we formulate a principled penalised optimisation problem to achieve sparse estimation of the inverse wavelet spectra of the time series, upon which our  $\mathcal{CIG}$  estimation procedure is built. We establish theoretical results showing that our  $\mathcal{CIG}$  estimator achieves desirable consistency properties, and demonstrate that the underlying conditional independence structure of the process can be successfully recovered.

Through a range of numerical experiments, we evaluated performance under different scenarios, including varying data-generating processes, graph structures, and data dimensions. We also proposed an agnostic procedure to recover the underlying graph of GNAR models from the estimated conditional independence graph. Finally, we applied the network estimation method to a dataset of COVID-19 patients in England and found spatial variation in graph density across the study area; the estimated underlying network improved forecasting performance in comparison to the user-defined adjacency built by [Nason et al. \(2025\)](#). A natural extension would be to adapt the wavelet-based TSglasso to nonstationary settings. This extension is non-trivial, as it requires careful definitions of network locally stationary processes and their conditional independence graphs, as well as their efficient aggregation.

**Disclosure Statement.** The authors report there are no competing interests to declare.

**Funding.** MAS is supported by a University of York doctoral scholarship. CB is supported by a scholarship from the EPSRC Centre for Doctoral Training in Statistical Applied Mathematics at Bath (SAMBa), under the project EP/S022945/1. MIK and MAN gratefully acknowledge support from EPSRC grant EP/X002195/1.

## References

Abadir, K. M. and Magnus, J. R. (2005), *Matrix Algebra*, Vol. 1, Cambridge University Press.

Abramovich, F., Bailey, T. C. and Sapatinas, T. (2000), ‘Wavelet analysis and its statistical applications’, *Journal of the Royal Statistical Society Series D* **49**(1), 1–29.

Akaike, H. (1974), ‘A new look at statistical model identification’, *IEEE Transactions on Automatic Control* **19**(6), 716–723.

Baek, C., Düker, M.-C. and Pipiras, V. (2023), ‘Local Whittle estimation of high-dimensional long-run variance and precision matrices’, *The Annals of Statistics* **51**(6), 2386–2414.

Billingsley, P. (1999), *Convergence of Probability Measures*, Wiley.

Böhm, H. and von Sachs, R. (2009), ‘Shrinkage estimation in the frequency domain of multivariate time series’, *Journal of Multivariate Analysis* **100**(5), 913–935.

Boyd, S., Parikh, N., Chu, E., Peleato, B., Eckstein, J. et al. (2011), ‘Distributed optimization and statistical learning via the alternating direction method of multipliers’, *Foundations and Trends® in Machine Learning* **3**(1), 1–122.

Brillinger, D. R. (1996), ‘Remarks concerning graphical models for time series and point processes’, *Brazilian Review of Econometrics* **16**(1), 1–23.

Brillinger, D. R. (2001), *Time series: Data Analysis and Theory*, SIAM.

Cerchiello, P. and Giudici, P. (2016), ‘Conditional graphical models for systemic risk estimation’, *Expert Systems with Applications* **43**, 165–174.

Chen, J. and Chen, Z. (2008), ‘Extended Bayesian information criteria for model selection with large model spaces’, *Biometrika* **95**(3), 759–771.

Dahlhaus, R. (2000), ‘Graphical interaction models for multivariate time series’, *Metrika* **51**(2), 157–172.

Dallakyan, A., Kim, R. and Pourahmadi, M. (2022), ‘Time series graphical lasso and sparse VAR estimation’, *Computational Statistics & Data Analysis* **176**, 107557.

Deb, N., Kuceyeski, A. and Basu, S. (2024), ‘Regularized estimation of sparse spectral precision matrices’, *arXiv preprint arXiv:2401.11128*.

Del Angel, M., Nunes, M., Peacock, O., Cranwell, E. and Thompson, D. (2025), ‘Analysing longitudinal wearable physical activity data using non-stationary time series models’, *International Journal of Behavioral Nutrition and Physical Activity* **22**(1), 88.

Dyrba, M., Mohammadi, R., Grothe, M. J., Kirste, T. and Teipel, S. J. (2020), ‘Gaussian graphical models reveal inter-modal and inter-regional conditional dependencies of brain alterations in alzheimer’s disease’, *Frontiers in Aging Neuroscience* **12**, 99.

Embleton, J., Knight, M. I. and Ombao, H. (2022), ‘Multiscale spectral modelling for nonstationary time series within an ordered multiple-trial experiment’, *Annals of Applied Statistics* **16**(4), 2774–2803.

Engelke, S. and Hitz, A. S. (2020), ‘Graphical models for extremes’, *Journal of the Royal Statistical Society Series B* **82**(4), 871–932.

Erdős, P. and Rényi, A. (1959), ‘On random graphs I’, *Publicationes Mathematicae* **6**, 290–297.

Fiecas, M., Leng, C., Liu, W. and Yu, Y. (2019), ‘Spectral analysis of high-dimensional time series’, *Electronic Journal of Statistics* **13**(2), 4079–4101.

Fiecas, M. and Ombao, H. (2011), ‘The generalized shrinkage estimator for the analysis of functional connectivity of brain signals’, *The Annals of Applied Statistics* **5**(2A), 1102 – 1125.

Fiecas, M., Ombao, H., Linkletter, C., Thompson, W. and Sanes, J. (2010), ‘Functional connectivity: Shrinkage estimation and randomization test’, *NeuroImage* **49**(4), 3005–3014.

Fiecas, M. and von Sachs, R. (2014), ‘Data-driven shrinkage of the spectral density matrix of a high-dimensional time series’, *Electronic Journal of Statistics* **8**, 2975–3003.

Friedman, J., Hastie, T. and Tibshirani, R. (2008), ‘Sparse inverse covariance estimation with the graphical lasso’, *Biostatistics* **9**(3), 432–441.

Friedman, J., Hastie, T. and Tibshirani, R. (2019), *glasso: Graphical Lasso: Estimation of Gaussian Graphical Models*. R package version 1.11.  
**URL:** <https://CRAN.R-project.org/package=glasso>

Gibberd, A. J. and Nelson, J. D. (2015a), Estimating dynamic graphical models from multivariate time-series data: Recent methods and results, in ‘International Workshop on Advanced Analytics and Learning on Temporal Data’, Springer, pp. 111–128.

Gibberd, A. J. and Nelson, J. D. (2015b), Estimating multiresolution dependency graphs within the stationary wavelet framework, in ‘2015 IEEE Global Conference on Signal and Information Processing (GlobalSIP)’, IEEE, pp. 547–551.

Hargreaves, J. K., Knight, M. I., Pitchford, J. W., Oakenfull, R. J. and Davis, S. J. (2018), ‘Clustering nonstationary circadian rhythms using locally stationary wavelet representations’, *Multiscale Modeling & Simulation* **16**(1), 184–214.

Hinne, M., Janssen, R. J., Heskes, T. and van Gerven, M. A. J. (2015), ‘Bayesian estimation of conditional independence graphs improves functional connectivity estimates’, *PLoS Computational Biology* **11**(11), e1004534.

Horn, R. and Johnson, C. (1985), *Matrix Analysis*, Cambridge University Press.

Jiménez-Varón, C. F. and Knight, M. I. (2025), ‘A GNAR-based framework for spectral estimation of network time series: Application to global bank network connectednesss’, *arXiv preprint arXiv:2510.06157*.

Johnson, S. (1967), ‘Hierarchical clustering schemes’, *Psychometrika* .

Jordan, M. I. (2004), ‘Graphical models’, *Statistical Science* **19**(1), 140–155.

Jung, A., Hannak, G. and Goertz, N. (2015), ‘Graphical lasso based model selection for time series’, *IEEE Signal Processing Letters* **22**(10), 1781–1785.

Kaufman, L. and Rousseeuw, P. J. (1987), Clustering by means of medoids, in ‘Statistical Data Analysis Based on the L1-Norm and Related Methods’, North-Holland, pp. 405–416.

Killick, R., Knight, M. I., Nason, G. P. and Eckley, I. A. (2020), ‘The local partial autocorrelation function and some applications’, *Electronic Journal of Statistics* **14**, 3268–3314.

Killick, R., Knight, M. I., Nason, G. P., Nunes, M. A. and Eckley, I. A. (2024), ‘Automatic locally stationary time series forecasting with application to predicting uk gross value added time series’, *Journal of the Royal Statistical Society Series C* **74**(1), 18–33.

Knight, M. I., Nunes, M. A. and Hargreaves, J. K. (2024), ‘Adaptive wavelet domain principal component analysis for nonstationary time series’, *Journal of Computational and Graphical Statistics* **33**(3), 941–954.

Knight, M. I., Nunes, M. and Nason, G. (2016), ‘Modelling, detrending and decorrelation of network time series’, *arXiv preprint arXiv:1603.03221* .

Knight, M., Leeming, K., Nason, G. and Nunes, M. (2020), ‘Generalised network autoregressive processes and the GNAR package’, *Journal of Statistical Software* **96**(5), 1–36.

Lauritzen, S. L. (1996), *Graphical Models*, Vol. 17, Clarendon Press.

Leeming, K., Nason, G., Nunes, M. A., Knight, M., Wei, J., Salnikov, D. and Borja, M. C. (2024), *GNAR: Methods for Fitting Network Time Series Models*. R package version 1.1.4. **URL:** <https://CRAN.R-project.org/package=GNAR>

Maathuis, M., Drton, M., Lauritzen, S. and Wainwright, M. (2018), *Handbook of Graphical Models*, CRC Press.

Magnus, J. and Neudecker, H. (1988), *Matrix Differential Calculus with Applications in Statistics and Econometrics*, Wiley series in probability and mathematical statistics, Wiley.

Matsuda, Y., Yajima, Y. and Tong, H. (2006), ‘Selecting models with different spectral density matrix structures by the cross-validated log likelihood criterion’, *Bernoulli* **12**(2), 221–249.

Nason, G. (2013), ‘A test for second-order stationarity and approximate confidence intervals for localized autocovariances for locally stationary time series’, *Journal of the Royal Statistical Society Series B* **75**(5), 879–904.

Nason, G. P. and Silverman, B. W. (1994), ‘The discrete wavelet transform in s’, *Journal of Computational and Graphical Statistics* **3**(2), 163–191.

Nason, G. P., Von Sachs, R. and Kroisandt, G. (2000), ‘Wavelet processes and adaptive estimation of the evolutionary wavelet spectrum’, *Journal of the Royal Statistical Society Series B* **62**(2), 271–292.

Nason, G., Salnikov, D. and Cortina-Borja, M. (2025), ‘New tools for network time series with an application to COVID-19 hospitalisations’, *Journal of the Royal Statistical Society Series A* p. qnaf182.

Ni, Y., Baladandayuthapani, V., Vannucci, M. and Stingo, F. C. (2022), ‘Bayesian graphical models for modern biological applications’, *Statistical Methods & Applications* **31**(2), 197–225.

Park, T., Eckley, I. A. and Ombao, H. C. (2014), ‘Estimating time-evolving partial coherence between signals via multivariate locally stationary wavelet processes’, *IEEE Transactions on Signal Processing* **62**(20), 5240–5250.

R Core Team (2024), *R: A Language and Environment for Statistical Computing*, R Foundation for Statistical Computing, Vienna, Austria.  
**URL:** <https://www.R-project.org/>

Ravikumar, P., Wainwright, M. J., Raskutti, G. and Yu., B. (2011), ‘High-dimensional covariance estimation by minimizing  $\ell_1$ -penalized log-determinant divergence’, *Electronic Journal of Statistics* **5**, 935–980.

Rothman, A. J., Bickel, P. J., Levina, E. and Zhu, J. (2008), ‘Sparse permutation invariant covariance estimation’, *Electronic Journal of Statistics* **2**, 494–515.

Schnabel, R. and Eskow, E. (1999), ‘A revised modified Cholesky factorization algorithm’, *SIAM J. Optim.* **9**(4), 1135–1148.

Schneider-Luftman, D. and Walden, A. T. (2016), ‘Partial coherence estimation via spectral matrix shrinkage under quadratic loss’, *IEEE Transactions on Signal Processing* **64**(22), 5767–5777.

Schwarz, G. (1978), ‘Estimating the dimension of a model’, *The Annals of Statistics* pp. 461–464.

Tugnait, J. K. (2022), ‘On sparse high-dimensional graphical model learning for dependent time series’, *Signal Processing* **197**, 108539.

Ubaru, S., Chen, J. and Saad, Y. (2017), ‘Fast estimation of  $tr(f(A))$  via stochastic Lanczos quadrature’, *SIAM Journal on Matrix Analysis and Applications* **38**(4), 1075–1099.

Wille, A. and Bühlmann, P. (2006), ‘Low-order conditional independence graphs for inferring genetic networks’, *Statistical Applications in Genetics and Molecular Biology* **5**(1).

Wilms, I., Basu, S., Bien, J. and Matteson, D. S. (2023), ‘Sparse identification and estimation of large-scale vector autoregressive moving averages’, *Journal of the American Statistical Association* **118**(541), 571–582.

Wu, H., Knight, M. I. and Ombao, H. (2023), ‘Multi-scale wavelet coherence with its applications’, *arXiv preprint arXiv:2305.10878*.

# A Proofs

In this appendix, we provide details of the proofs of the results established in the main text.

## A.1 Proof of Proposition 1

*Proof.* Akin to Wu et al. (2023), let us define a scale-dependent subprocess of the original process  $\mathbf{X}$  to be  $\mathbf{X}_{j,t} = (X_{j,t}^{(1)}, \dots, X_{j,t}^{(P)})^T$ , with the following representation,

$$\mathbf{X}_{j,t} = \sum_{k \in \mathbb{Z}} \mathbf{V}_j(k/T) \psi_{j,k}(t) \boldsymbol{\varepsilon}_{j,k} \quad (\text{A.1})$$

where the terms  $\mathbf{V}_j(k/T)$ ,  $\psi_{j,k}$  and  $\boldsymbol{\varepsilon}_{j,k}$  are as in the multivariate LSW definition. We can conceptualise the time series  $\{X_{j,t}^{(p)}\}_t$  as giving the scale- $j$  representation of the original node  $p$  process,  $\{X_t^{(p)}\}_t$ . From the zero-mean assumption for the innovations  $\{\boldsymbol{\varepsilon}_{j,k}\}_{j,k}$ , we immediately obtain that the subprocess is also zero-mean, i.e.  $\mathbb{E}(\mathbf{X}_{j,t}) = \mathbf{0}$ , at all times  $t$ . Coupling the zero-mean property with representation (A.1) yields

$$\begin{aligned} \mathbb{C}\text{ov}(X_{j,[uT]}^{(p)}, X_{j,[uT]+\tau}^{(q)}) &= \mathbb{E} \left[ X_{j,[uT]}^{(p)} X_{j,[uT]+\tau}^{(q)} \right] \\ &= \mathbb{E} \left[ \left( \sum_k \mathbf{V}_j^{(p)}(k/T) \psi_{j,k}([uT]) \boldsymbol{\varepsilon}_{j,k} \right) \times \left( \sum_{k'} \mathbf{V}_j^{(q)}(k'/T) \psi_{j,k'}([uT]+\tau) \boldsymbol{\varepsilon}_{j,k'} \right)^T \right] \\ &= \sum_k \sum_{k'} \mathbf{V}_j^{(p)}(k/T) \psi_{j,k}([uT]) \mathbb{E}(\boldsymbol{\varepsilon}_{j,k} \boldsymbol{\varepsilon}_{j,k'}^\top) \psi_{j,k'}([uT]+\tau) \left( \mathbf{V}_j^{(q)}(k'/T) \right)^T, \end{aligned}$$

where  $\mathbf{V}_j^{(p)}(u)$  denotes the  $p$ th row of  $\mathbf{V}_j(u)$ . From the assumptions on the innovation process, namely  $\mathbb{E}(\boldsymbol{\varepsilon}_{j,k} \boldsymbol{\varepsilon}_{j,k'}^\top) = \mathbb{C}\text{ov}(\boldsymbol{\varepsilon}_{j,k}, \boldsymbol{\varepsilon}_{j,k'}) = \delta_{j,j'} \delta_{k,k'} \mathbf{I}_P$ , with  $\mathbf{I}_P$  denoting the identity matrix, and using the definition of the LWS matrix,  $S_j^{(p,q)}(u) = \mathbf{V}_j^{(p)}(u) \left( \mathbf{V}_j^{(q)}(u) \right)^\top$ , by letting  $m = k - [uT]$  we obtain

$$\mathbb{C}\text{ov}(X_{j,[uT]}^{(p)}, X_{j,[uT]+\tau}^{(q)}) = \sum_m S_j^{(p,q)} \left( ([uT]+m)/T \right) \psi_{j,m}(0) \psi_{j,m}(\tau).$$

Define  $c_j^{(p,q)}(u, \tau) = S_j^{(p,q)}(u) \Psi_j(\tau)$  and, using the Lipschitz continuity of  $S_j^{(p,q)}(u)$ ,

$$\begin{aligned} &\left| \mathbb{C}\text{ov}(X_{j,[uT]}^{(p)}, X_{j,[uT]+\tau}^{(q)}) - c_j^{(p,q)}(u, \tau) \right| \\ &= \left| \sum_m S_j^{(p,q)} \left( ([uT]+m)/T \right) \psi_{j,m}(0) \psi_{j,m}(\tau) - c_j^{(p,q)}(u, \tau) \right| \\ &\leq T^{-1} \sum_m |m| L_j^{(p,q)} |\psi_{j,m}(0) \psi_{j,m}(\tau)| = \mathcal{O}(T^{-1}), \end{aligned}$$

where we used the scale- $j$  autocorrelation wavelet property of having a compact support of length  $2^j$ , coupled with  $\Psi_j(\tau) = \mathcal{O}(1)$  and the property of the Lipschitz constants.

Thus the process covariance is  $\mathbb{C}\text{ov}(X_{j,[uT]}^{(p)}, X_{j,[uT]+\tau}^{(q)}) \approx c_j^{(p,q)}(u, \tau)$ , which shows that under the assumption of stationarity of the original process  $\mathbf{X}$ , the covariance function of

the scale- $j$  subprocess is  $c_j^{(p,q)}(\tau) = S_j^{(p,q)}\Psi_j(\tau)$ ,  $\forall \tau$ . Also note that the process covariance is given by  $c^{(p,q)}(\tau) = \sum_j S_j^{(p,q)}\Psi_j(\tau)$  (Park et al., 2014), which can be reformulated using the subprocess notation as

$$c^{(p,q)}(\tau) = \sum_j c_j^{(p,q)}(\tau). \quad (\text{A.2})$$

Continuing under the process  $\mathbf{X}$  stationarity assumption, since the mean and covariance structures for the scale- $j$  subprocess are not time-dependent, as we have seen above, the scale-dependent subprocesses  $\{\mathbf{X}_{j,t}\}_t$  are themselves (weakly) stationary for each scale  $j$ .

In this setting, we can establish a relationship between the (Fourier) spectral density matrix and the stationary wavelet spectrum for each *subprocess*. Specifically, let  $\check{g}(\omega)$  denote the Fourier transform of  $g(\cdot)$ . Then for a node pair  $(p, q)$  and scale- $j$  subprocess  $\{\mathbf{X}_{j,t}\}_t$ , using linearity of the Fourier transform, we have the following relationship between the associated Fourier and wavelet spectra

$$f_j^{(p,q)}(\omega) = \check{c}_j^{(p,q)}(\omega) = S_j^{(p,q)}\check{\Psi}_j(\omega), \text{ for any frequency } \omega, \quad (\text{A.3})$$

where we denote by  $\mathbf{f}_j(\cdot)$  and  $\mathbf{S}_j$  the  $P \times P$ -dimensional Fourier and wavelet spectral matrices of the scale- $j$  subprocess, respectively. Then using (A.3), we obtain the precision matrix equivalent,

$$\mathbf{f}_j^{-1}(\omega) = \mathbf{S}_j^{-1}\check{\Psi}_j^{-1}(\omega), \forall \omega. \quad (\text{A.4})$$

If the nodal pair  $(p, q)$  is not associated to an edge in the conditional independence graph of the scale- $j$  subprocess, then by the results in Dahlhaus (2000) applied to the stationary subprocess  $\{\mathbf{X}_{j,t}\}_t$ , we have  $(\mathbf{f}_j^{-1}(\omega))_{p,q} = 0$  for all  $\omega$ , and (A.4) implies that  $(\mathbf{S}_j^{-1})_{p,q} = 0$ . This argument applies for every scale- $j$  subprocess, showing that the edge absence maps into a zero entry in the wavelet precision matrix at each scale. Conversely, if we set  $(\mathbf{S}_j^{-1})_{p,q} = 0$ , then the right-hand side of (A.4) vanishes and  $(\mathbf{f}_j^{-1}(\omega))_{p,q} = 0$  for all  $\omega$ , which again by Dahlhaus (2000) means that there is no  $(p, q)$  edge in the conditional independence structure of the scale- $j$  subprocess.

We next show that the conditional independence of two nodes given the remaining ones is equivalent to the conditional independence of their subprocesses across all scales  $j$ . Let us denote by  $\{e_t^{(p)}\}_t$  the channel  $p$  residual process obtained by removing the linear effects of the nodes other than  $p, q$  from the original process  $\mathbf{X}$  and  $\{e_{j,t}^{(p)}\}$  denote the corresponding residual subprocess at scale- $j$ ; similarly, define the residual process at node  $q$  and its associated subprocesses. Following the arguments in Dahlhaus (2000), the process  $\{(e_t^{(p)}, e_t^{(q)})^\top\}_t$  is bivariate stationary, and the Fourier and wavelet cross-spectra of their scale  $j$ -subprocess are connected akin to equation (A.3), namely

$$f_j^{e;(p,q)}(\omega) = S_j^{e;(p,q)}\check{\Psi}_j(\omega). \quad (\text{A.5})$$

Additionally, following (A.2) for the residual process, we may express its covariance using the covariances of the residual subprocesses as

$$c^{e;(p,q)}(\tau) = \sum_j c_j^{e;(p,q)}(\tau) = \sum_j S_j^{e;(p,q)}\Psi_j(\tau), \forall \tau. \quad (\text{A.6})$$

Now recall the fact that the nodal pair  $(p, q)$  is not associated to an edge in the conditional independence graph of the process  $\mathbf{X}$  means that  $c^{e;(p,q)}(\tau) = 0$ ,  $\forall \tau$  (Dahlhaus, 2000). Then

the linear independence of the autocorrelation wavelets and (A.6) translate into  $S_j^{e;(p,q)} = 0, \forall j$  (see e.g. the proof of Theorem 1 of [Nason et al. \(2000\)](#)). Coupled with (A.5) for the residual subprocess, we obtain that

$$f_j^{e;(p,q)}(\omega) = 0, \forall \omega, \forall j$$

which is equivalent in the Dahlhaus sense to the conditional independence of the nodes  $p$  and  $q$  for the subprocesses across all scales  $j$ . The same argument follows in the opposite direction, hence the conditional independence graphs coincide across all scales.  $\square$

## A.2 Proof of Theorem 1

Our proof of Theorem 1 follows the general strategy of [Ravikumar et al. \(2011\)](#) and [Tugnait \(2022\)](#) but is adapted to the wavelet-domain likelihood and scale-wise formulation. We first obtain a high-probability bound for the deviation of the spectral estimator (Lemmas 1–2), then develop a Taylor expansion for the log-determinant with explicit integral remainder (Lemmas 3–4), and finally combine these to obtain a bound on the Frobenius norm of  $\hat{\Theta}_j - \Theta_{0j}$ . Note that in the below, for notational simplicity we drop the dependency on the scale  $j$  in the bounding constants.

Lemma 1 provides a tail bound for entries of a sample covariance matrix of a Gaussian vector and is taken from [Ravikumar et al. \(2011\)](#) where a proof is given.

**Lemma 1.** *Consider a zero-mean Gaussian random vector  $\mathbf{z} \in \mathbb{R}^P$  with covariance matrix  $\mathbf{c}_z \succ \mathbf{0}$ . Given  $T$  independent, identically distributed (iid) samples  $\mathbf{z}_t, t = 0, \dots, T-1$  of  $\mathbf{z}$ , let  $\hat{\mathbf{c}}_z = (1/T) \sum_{t=0}^{T-1} \mathbf{z}_t \mathbf{z}_t^T$  denote the sample covariance matrix. Then  $\hat{\mathbf{c}}_z$  satisfies the tail bound*

$$\mathbb{P}\left(|(\hat{\mathbf{c}}_z - \mathbf{c}_z)_{p,q}| > \delta\right) \leq 4 \exp\left(-\frac{T\delta^2}{3200 \max_p(c_{z;p,p}^2)}\right)$$

for all  $\delta \in (0, 40 \max_p(\mathbf{c}_{z;p,p}))$ , for any  $p, q = 1, \dots, P$ .

Lemma 2 applies Lemma 1 to the wavelet spectral estimator  $\hat{\mathbf{S}}_j$  at a fixed scale  $j$ .

**Lemma 2.** *Under Assumption 1 in Section 3.1.3, the smoothed periodogram  $\bar{\mathbf{I}}_j^{(Y)}$  used as an estimator of  $\mathbf{S}_j^{(X)}$  in the optimisation problem (9), here denoted as  $\hat{\mathbf{S}}_j^{(X)}$ , satisfies the tail bound*

$$\mathbb{P}\left(\max_{p,q} |(\hat{\mathbf{S}}_j^{(X)} - \mathbf{S}_{0j}^{(X)})_{p,q}| > C_0 \sqrt{\frac{\log(P_T)}{T}}\right) \leq \frac{1}{P_T^{\nu-2}},$$

for  $\nu > 2$  if  $T$  is such that  $T > N_1 = 2 \log(4P_T^\nu)$  and  $C_0 = \left(40 \max_p (\mathbf{S}_{0j}^{(X)})_{p,p}\right) \sqrt{\frac{N_1}{\log(P_T)}}$ , where we recall that  $P_T$  denotes the dimension of the process, allowed to increase with  $T$ .

*Proof.* Recall that for each scale  $j$ , we have  $\mathbb{E}(\mathbf{d}_{j,k}^{(Y)} (\mathbf{d}_{j,k}^{(Y)})^\top) \approx \mathbf{S}_{0j}^{(X)}$ ,  $\forall k$  from equation (8) and  $\mathbf{d}_{j,k}^{(Y)} \sim N_{P_T}(\mathbf{0}, \mathbf{S}_{0j}^{(X)})$ , where  $\mathbf{S}_{0j}^{(X)}$  denotes the true spectrum of  $\mathbf{X}$ .

Under stationarity, we have that  $\hat{\mathbf{S}}_j^{(X)} = \frac{1}{T} \sum_{k=0}^{T-1} \mathbf{I}_{j,k}^{(Y)} = \frac{1}{T} \sum_{k=0}^{T-1} \mathbf{d}_{j,k}^{(Y)} (\mathbf{d}_{j,k}^{(Y)})^\top$  and using the approximate uncorrelatedness of the wavelet coefficients coupled with the process Gaussianity, we apply Lemma 1 with  $\mathbf{z} := \mathbf{d}_{j,k}^{(Y)}$  and  $\mathbf{c}_z := \mathbf{S}_{0j}^{(X)}$  to obtain for all  $\delta \in (0, 40 \max_p (\mathbf{S}_{0j}^{(X)})_{p,p})$

$$\mathbb{P}(|(\hat{\mathbf{S}}_j^{(X)} - \mathbf{S}_{0j}^{(X)})_{p,q}| > \delta) \leq 4 \exp\left(-\frac{T\delta^2}{3200 \max_p ((\mathbf{S}_{0j}^{(X)})_{p,p}^2)}\right).$$

Taking a union bound over the  $P_T^2$  entries of the matrix  $[\hat{\mathbf{S}}_j^{(X)} - \mathbf{S}_{0j}^{(X)}]$  for a fixed  $j$  yields

$$\mathbb{P}\left(\max_{p,q} |(\hat{\mathbf{S}}_j^{(X)} - \mathbf{S}_{0j}^{(X)})_{p,q}| > \delta\right) \leq 4P_T^2 \exp\left(-\frac{T\delta^2}{3200 \max_p ((\mathbf{S}_{0j}^{(X)})_{p,p}^2)}\right) := \kappa,$$

for  $\delta \in (0, 40 \max_p (\mathbf{S}_{0j}^{(X)})_{p,p})$ .

Letting  $\delta := C_0 \sqrt{\frac{\log(P_T)}{T}}$ , with  $C_0$  as in the statement of the lemma, fulfils the condition  $\delta \in (0, 40 \max_p (\mathbf{S}_{0j}^{(X)})_{p,p})$  due to the construction  $N_1 < T$ . Additionally, since the auto-spectrum entries  $(\mathbf{S}_{0j}^{(X)})_{p,p}$  are all positive (hence the maximum of their squares is just the squared maximum), we use  $N_1 = 2 \log(4P_T^\nu)$ , and rearrange to obtain  $\kappa = P_T^{2-\nu}$ , as desired. (To aid manipulations, we may denote  $c_* = (40 \max_p (\mathbf{S}_{0j}^{(X)})_{p,p})^{-1}$  so that  $\kappa = 4P_T^2 \exp\left(-\frac{\delta^2 T c_*^2}{2}\right)$  and note that  $c_* \delta = \sqrt{\frac{2 \log(4P_T^\nu)}{T}} = \sqrt{\frac{N_1}{T}}$ , thus  $\kappa = \frac{1}{P_T^{\nu-2}}$ .)  $\square$

**Notational Simplifications.** From here on, we will drop the explicit notation showing to which process standard quantities pertain: going forward  $\Theta_j$  denotes  $\Theta_j^{(X)}$ ;  $\mathbf{S}_j$  denotes  $\mathbf{S}_j^{(X)}$ , and we will also write  $\mathbf{d}_{j,k}$  to denote  $\mathbf{d}_{j,k}^{(Y)}$ ;  $\bar{\mathbf{I}}_j$  to denote  $\bar{\mathbf{I}}_j^{(Y)}$ , unless otherwise stated.

Next, Lemma 3 gives a second-order Taylor expansion for terms of the form  $\log \det(\Theta_0 + \Delta)$ , for some matrix  $\Delta$ .

**Lemma 3.** *At each scale  $j$ , denote  $g(\Theta_j) = \log \det(\Theta_j)$  and let  $\Theta_j = \Theta_{0j} + \Delta_j$ , with  $\Delta_j^\top = \Delta_j$ . Then the Taylor series expansion of  $g(\Theta_j)$  at  $\Theta_{0j}$  is given by*

$$g(\Theta_j) = g(\Theta_{0j}) + \text{tr}(\Theta_{0j}^{-1} \Delta_j) - \frac{1}{2} \text{vec}(\Delta_j)^\top (\Theta_{0j}^{-1} \otimes \Theta_{0j}^{-1}) \text{vec}(\Delta_j) + \text{h.o.t}, \quad (\text{A.7})$$

where the acronym h.o.t stands for higher order terms in  $\Delta_j$ .

*Proof.* In the notation above,  $g(\Theta_j) = \log \det(\Theta_{0j} + \Delta_j)$ . Note that using the invertibility of the spectra/precision matrices, we can write

$$\Theta_{0j} + \Delta_j = \Theta_{0j}^{1/2} (\mathbf{I}_{P_T} + \Theta_{0j}^{-1/2} \Delta_j \Theta_{0j}^{-1/2}) \Theta_{0j}^{1/2}, \quad (\text{A.8})$$

where  $\mathbf{I}_{P_T}$  denotes the identity matrix of size  $P_T \times P_T$ . As all matrices are square, using basic properties of determinants we obtain

$$\begin{aligned} \det(\Theta_{0j} + \Delta_j) &= \det(\Theta_{0j}) \det(\mathbf{I}_{P_T} + \Theta_{0j}^{-1/2} \Delta_j \Theta_{0j}^{-1/2}), \text{ from which we derive} \\ \log \det(\Theta_{0j} + \Delta_j) &= \log \det(\Theta_{0j}) + \log \det(\mathbf{I}_{P_T} + \mathbf{U}), \end{aligned} \quad (\text{A.9})$$

where to simplify notation we use  $\mathbf{U} = \Theta_{0j}^{-1/2} \Delta_j \Theta_{0j}^{-1/2}$ .

Focusing on the second term in the right-hand side of equation (A.9), we have  $\log \det(\mathbf{I}_{P_T} + \mathbf{U}) = \text{tr}(\log(\mathbf{I}_{P_T} + \mathbf{U}))$  (Ubaru et al., 2017) since  $(\mathbf{I}_{P_T} + \mathbf{U})$  is symmetric and positive definite. The symmetry follows immediately from the definition of  $\mathbf{U}$  and the symmetry of the precision matrices. The positive definiteness follows by observing that (A.8) can be re-written as  $\mathbf{I}_{P_T} + \mathbf{U} = \Theta_{0j}^{-1/2} \Delta_j \Theta_{0j}^{-1/2}$ , where the precision matrix  $\Theta_j$  is positive definite as the inverse of a positive definite matrix, the scale- $j$  spectrum  $\mathbf{S}_j$ .

Hence we can use a Taylor expansion to write  $\log \det(\mathbf{I}_{P_T} + \mathbf{U}) = \text{tr}(\mathbf{U}) - \frac{1}{2}\text{tr}(\mathbf{U}^2) + \text{h.o.t.}$ , which coupled with equation (A.9) yields

$$\log \det(\Theta_{0j} + \Delta_j) = \log \det(\Theta_{0j}) + \text{tr}(\mathbf{U}) - \frac{1}{2}\text{tr}(\mathbf{U}^2) + \text{h.o.t.} \quad (\text{A.10})$$

Considering each term separately, we have

$$\text{tr}(\mathbf{U}) = \text{tr}(\Theta_{0j}^{-1/2} \Delta_j \Theta_{0j}^{-1/2}) = \text{tr}(\Theta_{0j}^{-1} \Delta_j), \text{ since } \text{tr}(\mathbf{ABC}) = \text{tr}(\mathbf{BCA}), \quad (\text{A.11})$$

$$\begin{aligned} \text{tr}(\mathbf{U}^2) &= \text{tr}(\Theta_{0j}^{-1/2} \Delta_j \Theta_{0j}^{-1} \Delta_j \Theta_{0j}^{-1/2}) \\ &= \text{tr}(\Theta_{0j}^{-1} \Delta_j \Theta_{0j}^{-1} \Delta_j) \\ &= \text{vec}(\Delta_j)^\top (\Theta_{0j}^{-1} \otimes \Theta_{0j}^{-1}) \text{vec}(\Delta_j), \end{aligned} \quad (\text{A.12})$$

where for the last equality we used the relationship  $\text{tr}(\mathbf{ABCD}) = \text{vec}(\mathbf{D}^\top)^\top (\mathbf{C}^\top \otimes \mathbf{A}) \text{vec}(\mathbf{B})$  (Abadir and Magnus, 2005, Chapter 10.2) and the symmetry of  $\Delta_j$ .

Replacing equations (A.11) and (A.12) into equation (A.10), we have

$$g(\Theta_j) = g(\Theta_{0j}) + \text{tr}(\Theta_{0j}^{-1} \Delta_j) - \frac{1}{2} \text{vec}(\Delta_j)^\top (\Theta_{0j}^{-1} \otimes \Theta_{0j}^{-1}) \text{vec}(\Delta_j) + \text{h.o.t.}, \quad (\text{A.13})$$

where we have also used  $g(\Theta_{0j}) = \log \det(\Theta_{0j})$ .  $\square$

Lemma 4 refines the expansion in Lemma 3 to an integral remainder form to aid bounding.

**Lemma 4.** *With  $g(\Theta_j) = \log \det(\Theta_j)$  and  $\Theta_j = \Theta_{0j} + \Delta_j$  defined as in Lemma 3 at each scale  $j$ , the Taylor series expansion of  $g(\Theta_j)$  in integral remainder form is given by*

$$g(\Theta_j) = g(\Theta_{0j}) + \text{tr}(\Theta_{0j}^{-1} \Delta_j) - \text{vec}(\Delta_j)^\top \left[ \int_0^1 (1-v) H(\Theta_{0j}, \Delta_j, v) dv \right] \text{vec}(\Delta_j), \quad (\text{A.14})$$

where  $H(\Theta_{0j}, \Delta_j, v) = ((\Theta_{0j} + v\Delta_j)^{-1})^\top \otimes (\Theta_{0j} + v\Delta_j)^{-1}$  and we use the usual notation,  $\text{vec}(\Delta_j)$  for the operator that stacks the columns of the matrix  $\Delta_j$ ;  $\otimes$  for the Kronecker product, see e.g. Abadir and Magnus (2005).

*Proof.* Using the integral form of the remainder for the Taylor expansion of a function  $h(\cdot)$ , we have

$$h(1) = h(0) + h'(0) + \int_0^1 (1-v) h''(v) dv. \quad (\text{A.15})$$

Let  $h(v) := g(\Theta_{0j} + v\Delta_j)$ , and we denote  $\Theta(v) = \Theta_{0j} + v\Delta_j$  for  $v \in [0, 1]$ .

Then  $h(0) = \log \det(\Theta_{0j})$ ,  $h(1) = \log \det(\Theta_{0j} + \Delta_j)$ , and

$$\begin{aligned} h'(v) &= \frac{d}{dv} g(\Theta_{0j} + v\Delta_j) \\ &= \text{tr} \left( \Theta(v)^{-1} \frac{d}{dv} \Theta(v) \right) \\ &= \text{tr} (\Theta(v)^{-1} \Delta_j), \end{aligned}$$

where the second equality follows from Jacobi's identity (Magnus and Neudecker, 1988) and  $\frac{d}{dv} \Theta(v) = \Delta_j$ . Hence we obtain  $h'(0) = \text{tr}(\Theta_{0j}^{-1} \Delta_j)$ .

For the second derivative,  $h''(v) = \frac{d}{dv} \text{tr}(\Theta(v)^{-1} \Delta_j)$ , thus  $h''(v) = \text{tr} \left( \frac{d}{dv} (\Theta(v)^{-1}) \Delta_j \right)$  and we first find  $\frac{d}{dv} (\Theta(v)^{-1})$ . This follows from  $\frac{d}{dv} (\Theta(v) \Theta(v)^{-1}) = \frac{d}{dv} \mathbf{I}_{P_T} = \mathbf{0}_{P_T}$  which gives

$$\frac{d}{dv} (\Theta(v)^{-1}) = -\Theta(v)^{-1} \left( \frac{d}{dv} \Theta(v) \right) \Theta(v)^{-1}.$$

Hence,

$$\begin{aligned} h''(v) &= -\text{tr} \left( \Theta(v)^{-1} \left( \frac{d}{dv} \Theta(v) \right) \Theta(v)^{-1} \Delta_j \right) \\ &= -\text{vec}(\Delta_j^\top)^\top ((\Theta(v)^{-1})^\top \otimes \Theta(v)^{-1}) \text{vec}(\Delta_j) \\ &= -\text{vec}(\Delta_j)^\top H(\Theta_{0j}, \Delta_j, v) \text{vec}(\Delta_j), \end{aligned}$$

where we have used  $\frac{d}{dv} \Theta(v) = \Delta_j$  in the second equality and  $\text{tr}(\mathbf{ABCD}) = \text{vec}(\mathbf{D}^\top)^\top (\mathbf{C}^\top \otimes \mathbf{A}) \text{vec}(\mathbf{B})$ . We are now in position to replace each component into equation (A.15) and obtain

$$\begin{aligned} g(\Theta_j) &= g(\Theta_{0j}) + \text{tr}(\Theta_{0j}^{-1} \Delta_j) \\ &\quad - \int_0^1 (1-v) \text{vec}(\Delta_j)^\top H(\Theta_{0j}^{-1}, \Delta_j, v) \text{vec}(\Delta_j) dv \\ &= \log \det(\Theta_{0j}) + \text{tr}(\Theta_{0j}^{-1} \Delta_j) \\ &\quad - \text{vec}(\Delta_j)^\top \left( \int_0^1 (1-v) H(\Theta_{0j}^{-1}, \Delta_j, v) dv \right) \text{vec}(\Delta_j). \end{aligned}$$

□

## Proof of Theorem 1

*Proof.* Recall the objective function in the optimisation problem (9) is

$$\mathcal{L}(\Theta_j) = -T[\log \det(\Theta_j) - \text{tr}(\bar{\mathbf{I}}_j \Theta_j)] + \mathcal{P}(\Theta_j, \lambda_j), \forall j$$

where we write  $\Theta_j$  to denote  $\Theta_j^{(X)}$  and  $\bar{\mathbf{I}}_j$  to denote  $\bar{\mathbf{I}}_j^{(Y)}$  for notational simplicity. Dropping the dependence on  $j$ , we equivalently define

$$\tilde{\mathcal{L}}(\Theta) = \frac{\mathcal{L}(\Theta)}{T} = -\log \det(\Theta) + \text{tr}(\bar{\mathbf{I}} \Theta) + \lambda' \|\Theta^-\|_1,$$

where  $\lambda' = \lambda/T$  and  $\Theta^-$  denotes the off-diagonal entries of  $\Theta$ . Set  $\Delta = \Theta - \Theta_0$  and define

$$\mathcal{Q}(\Delta) := \tilde{\mathcal{L}}(\Theta_0 + \Delta) - \tilde{\mathcal{L}}(\Theta_0).$$

The estimate  $\hat{\Theta}$  minimizes  $\mathcal{L}(\Theta)$ , or equivalently  $\tilde{\mathcal{L}}(\Theta)$ , and therefore  $\hat{\Delta} = \hat{\Theta} - \Theta_0$  minimizes  $\mathcal{Q}(\Delta)$ .

Following the argument in [Tugnait \(2022\)](#), if we can show that with high probability

$$\inf_{\|\Delta\|_F = Rr_T} \mathcal{Q}(\Delta) > 0,$$

then the minimizer  $\hat{\Delta} = \hat{\Theta} - \Theta_0$  is such that  $\|\hat{\Delta}\|_F \leq Rr_T$ . It would therefore follow that

$$\|\hat{\Theta} - \Theta_0\|_F \leq Rr_T.$$

This argument follows from the proof of Theorem 1 from [Rothman et al. \(2008\)](#). We now express  $\mathcal{Q}(\Delta)$  in terms of  $\Theta$  and  $\Delta$ :

$$\begin{aligned} \mathcal{Q}(\Delta) &= \text{tr}(\bar{\mathbf{I}}\Delta) - [\log \det(\Theta_0 + \Delta) - \log \det(\Theta_0)] \\ &\quad + \lambda'[\|\Theta_0^- + \Delta^-\|_1 - \|\Theta_0^-\|_1]. \end{aligned}$$

Recall that our construction in Section 3.1 ensures that the periodogram of the process  $\mathbf{Y}$  is an asymptotically unbiased estimator of the target spectrum of the process  $\mathbf{X}$ , see equation (8), namely under stationarity we have  $\mathbb{E}(\bar{\mathbf{I}}^{(Y)}) \approx \beta^{(Y)} = \mathbf{S}^{(X)}$ , and hence  $\bar{\mathbf{I}}^{(Y)}$  is an estimate for  $\mathbf{S}^{(X)}$  and so in what follows we write  $\hat{\mathbf{S}}$  to replace  $\bar{\mathbf{I}}$ . Let  $\mathbf{S}_0 = \Theta_0^{-1}$  denote the true wavelet spectrum.

Let us split the spectral estimator as  $\hat{\mathbf{S}} = \mathbf{S}_0 + (\hat{\mathbf{S}} - \mathbf{S}_0)$  which gives  $\text{tr}(\Delta\bar{\mathbf{I}}) = \text{tr}(\Delta\mathbf{S}_0) + \text{tr}(\Delta(\hat{\mathbf{S}} - \mathbf{S}_0))$  and leads us to splitting the objective function into three parts

$$\begin{aligned} \mathcal{Q}(\Delta) &= A_1 + A_2 + A_3, \text{ where} \\ A_1 &:= \text{tr}(\mathbf{S}_0\Delta) - \log \det(\Theta_0 + \Delta) + \log \det(\Theta_0), \\ A_2 &:= \text{tr}((\hat{\mathbf{S}} - \mathbf{S}_0)\Delta), \\ A_3 &:= \lambda'(\|\Theta_0^- + \Delta^-\|_1 - \|\Theta_0^-\|_1). \end{aligned}$$

Our next aim is to lower bound each of the three terms  $A_1$ ,  $A_2$  and  $A_3$  in order to show that  $\mathcal{Q}(\Delta) > 0$  when  $\Delta$  is such that  $\|\Delta\|_F = Rr_T$ . Let us first bound  $A_3$ .

Using the edge set notation  $\mathcal{E}_0$  from Assumption 2 and denoting by  $\mathcal{E}_0^c$  its complement, we split the matrix  $\Delta$  into matrices  $\Delta_{\mathcal{E}_0}$  and  $\Delta_{\mathcal{E}_0^c}$ , where  $(\Delta_{\mathcal{E}_0})_{p,q} = (\Delta)_{p,q}$  if  $(p, q) \in \mathcal{E}_0$  and 0 otherwise, and similarly for the edge complement set. Hence  $\Delta^- = \Delta_{\mathcal{E}_0} + \Delta_{\mathcal{E}_0^c}^-$ , and

$$\begin{aligned} A_3 &= \lambda'(\|\Theta_0^- + \Delta^-\|_1 - \|\Theta_0^-\|_1) \\ &= \sum_{p,q \in \mathcal{E}_0} \lambda'(\|(\Theta_0)_{p,q}^- + (\Delta)_{p,q}^-\|_1 - \|(\Theta_0)_{p,q}^-\|_1) \\ &\quad + \sum_{p,q \in \mathcal{E}_0^c} \lambda'(\|(\Theta_0)_{p,q}^- + (\Delta)_{p,q}^-\|_1 - \|(\Theta_0)_{p,q}^-\|_1). \end{aligned}$$

Since  $(\Theta_0)_{p,q} = 0$  if  $(p, q) \notin \mathcal{E}_0$ , we have,

$$\begin{aligned} A_3 &= \sum_{p,q \in \mathcal{E}_0} \lambda'(\|(\Theta_0^-)_{p,q} + (\Delta^-)_{p,q}\|_1 - \|(\Theta_0^-)_{p,q}\|_1) + \lambda' \|\Delta_{\mathcal{E}_0^c}^-\|_1 \\ &= \lambda' (\|\Theta_0^- + \Delta_{\mathcal{E}_0}^-\|_1 - \|\Theta_0^-\|_1) + \lambda' (\|\Delta_{\mathcal{E}_0^c}^-\|_1) \\ &\geq \lambda' (-\|\Delta_{\mathcal{E}_0}^-\|_1) + \lambda' (\|\Delta_{\mathcal{E}_0^c}^-\|_1), \text{ by the triangle inequality.} \end{aligned}$$

Hence we have,

$$A_3 \geq \lambda' (\|\Delta_{\mathcal{E}_0^c}^-\|_1 - \|\Delta_{\mathcal{E}_0}^-\|_1).$$

Turning to  $A_1$ , using Lemma 4 this term can be equivalently written as

$$A_1 = \text{vec}(\Delta)^\top K(\Theta_0, \Delta) \text{vec}(\Delta),$$

where  $K(\Theta_0, \Delta) = \int_0^1 (1-v) H(\Theta_0, \Delta, v) dv$ , with  $H(\Theta_0, \Delta, v)$  defined as in Lemma 4.

Using the notation therein, recall that  $\Theta(v) = \Theta_0 + v\Delta$  with  $v \in [0, 1]$  fixed. By Assumption 3 on the conditions on the boundedness of the eigenvalues of  $\Theta_0$ , coupled with Weyl's identity (Horn and Johnson, 1985), we obtain that all eigenvalues of  $\Theta(v)$  must lie within the interval  $[\tilde{\phi}_{\min}, \tilde{\phi}_{\max}]$  where  $\tilde{\phi}_{\min} \geq \phi_{\min} - \eta$  and  $\tilde{\phi}_{\max} \leq \phi_{\max} + \eta$  and  $\eta = \|\Delta\|_2$ .

Hence, the eigenvalues of  $\Theta(v)^{-1}$  are contained within  $[\tilde{\phi}_{\max}^{-1}, \tilde{\phi}_{\min}^{-1}]$ . Given that  $H(\Theta_0, \Delta, v) = (\Theta(v)^{-1})^\top \otimes \Theta(v)^{-1}$ , the eigenvalues of  $H(\Theta_0, \Delta, v)$  are such that  $\phi_{\min}(H(\Theta_0, \Delta, v)) \geq \tilde{\phi}_{\max}^{-2}$ . Therefore  $H(\Theta_0, \Delta, v) - \tilde{\phi}_{\max}^{-2} \mathbf{I}_{P_T}$  is positive semi-definite, where  $\mathbf{I}_{P_T}$  denotes the identity matrix with dimension  $P_T$ . This in turn yields

$$\begin{aligned} A_1 &\geq \text{vec}(\Delta)^\top \left( \int_0^1 (1-v) \tilde{\phi}_{\max}^{-2} \mathbf{I}_{P_T} dv \right) \text{vec}(\Delta) \\ &= \frac{\tilde{\phi}_{\max}^{-2}}{2} \text{vec}(\Delta)^\top \mathbf{I}_{P_T} \text{vec}(\Delta) \\ &= \frac{\tilde{\phi}_{\max}^{-2}}{2} \|\text{vec}(\Delta)\|_2^2 \\ &= \frac{\tilde{\phi}_{\max}^{-2}}{2} \|\Delta\|_F^2 \\ &= c_1 \|\Delta\|_F^2, \text{ with } c_1 = \frac{\tilde{\phi}_{\max}^{-2}}{2}. \end{aligned} \tag{A.16}$$

Moving on to the term  $A_2$  which can be equivalently written as  $A_2 = \sum_{p,q} (\hat{\mathbf{S}} - \mathbf{S}_0)_{p,q} \Delta_{q,p}$  and applying Lemma 2, we can see that

$$\max_{p,q} |(\hat{\mathbf{S}} - \mathbf{S}_0)_{p,q}| \leq C_0 \sqrt{\frac{\log(P_T)}{T}}$$

with high probability  $(1 - \frac{1}{P_T^{\nu-2}})$ . So,

$$|A_2| \leq C_0 \sqrt{\frac{\log(P_T)}{T}} \sum_{p,q} |\Delta|_{q,p} = C_0 \sqrt{\frac{\log(P_T)}{T}} \|\Delta\|_1. \tag{A.17}$$

As there are  $P_T^2$  entries in the matrix  $\Delta$ , it follows that  $\|\Delta\|_1 \leq P_T \|\Delta\|_F$  by the Cauchy-Schwarz inequality. Coupled with (A.17), we obtain

$$|A_2| \leq C_0 \sqrt{\frac{\log(P_T)}{T}} P_T \|\Delta\|_F = C_0 r_T \|\Delta\|_F,$$

where  $r_T = P_T \sqrt{\frac{\log(P_T)}{T}}$  and we have the following lower bound for  $A_2$ :

$$A_2 \geq -C_0 r_T \|\Delta\|_F. \quad (\text{A.18})$$

We now consider the term  $A_3$ . We have  $A_3 \geq \lambda'(\|\Delta_{\mathcal{E}_0^-}\|_1 - \|\Delta_{\mathcal{E}_0}\|_1) \geq -\lambda' \|\Delta_{\mathcal{E}_0^-}\|_1$ , since the first term is non-negative. Hence similarly to  $A_2$  we can write

$$A_3 \geq -\lambda' \sqrt{E_{0T}} \|\Delta\|_F, \quad (\text{A.19})$$

since there are  $E_{0T}$  non-zero values in  $\mathcal{E}_0$  by Assumption 2.

Putting together all three lower bounds in equations (A.16), (A.18) and (A.19), we obtain

$$\begin{aligned} \mathcal{Q}(\Delta) &\geq c_1 \|\Delta\|_F^2 - C_0 r_T \|\Delta\|_F - \lambda' \sqrt{E_{0T}} \|\Delta\|_F \\ &= r_T (c_1 R^2 r_T - C_0 R r_T - \lambda' \sqrt{E_{0T}} R) \\ &\geq r_T (c_1 R^2 r_T - C_0 R r_T - C_1 \frac{r_T}{P_T} \sqrt{E_{0T}} R) \\ &= r_T^2 \left( c_1 R^2 - C_0 R - C_1 \frac{\sqrt{E_{0T}}}{P_T} R \right) \\ &\geq r_T^2 (c_1 R^2 - (C_0 + C_1) R), \end{aligned}$$

where we used matrices  $\Delta$  such that  $\|\Delta\|_F = R r_T$ . The last inequality follows from Assumption 2 sparsity constraint, namely  $E_{0T} \ll P_T(P_T - 1)$ , thus  $\frac{\sqrt{E_{0T}}}{P_T} \leq 1$ . Hence from Lemma 2, we obtain  $\mathcal{Q}(\Delta) > 0$  with high probability if  $R$  is such that  $R > \frac{C_0 + C_1}{c_1} =: \tilde{C}$ , so we let  $R = \tilde{C} + \delta$ , for  $\delta > 0$ .

Therefore with at least probability  $(1 - 1/P_T^{\nu-2})$ , no minimiser of  $\tilde{\mathcal{L}}(\Theta_j)$  (and therefore of  $\mathcal{L}(\Theta_j)$ ) can lie outside the Frobenius ball of radius  $R r_T$  around  $\Theta_{0j}$ , which implies that

$$\|\hat{\Theta} - \Theta_0\|_F = \mathcal{O}_p(R r_T).$$

This yields the claimed  $\mathcal{O}_p(R r_T)$  bound. □

### A.3 Proof of Proposition 2

*Proof.* Consider the  $\mathcal{CIG}$ s for two scales  $j_1$  and  $j_2$ . From Proposition 1, the  $\mathcal{CIG}$ s across scales  $j$  coincide, i.e., for a pair of nodes  $(p, q)$  corresponding to no edge in the conditional independence graph of the process, we have  $(\mathbf{f}_{j_1}^{-1}(\omega))_{p,q} = 0$  and  $(\mathbf{f}_{j_2}^{-1}(\omega))_{p,q} = 0$  for all frequencies  $\omega$  and fixed scales  $j_1, j_2$ . This is equivalent to the sum of their modulus  $|(\mathbf{f}_{j_1}^{-1}(\omega))_{p,q}| + |(\mathbf{f}_{j_2}^{-1}(\omega))_{p,q}| = 0$  for all  $\omega$ , which in turn is equivalent to (see proof of Theorem 1)  $|(\Theta_{j_1})_{p,q}| + |(\Theta_{j_2})_{p,q}| = 0$ .

Since Theorem 1 establishes consistency of  $\hat{\Theta}_{j_1}$  and  $\hat{\Theta}_{j_2}$ , by the continuous mapping theorem applied to the bivariate random variable  $(\hat{\Theta}_{j_1}, \hat{\Theta}_{j_2})$  with the function  $f(x, y) \rightarrow |x| + |y|$ , we obtain that  $|(\hat{\Theta}_{j_1})_{p,q}| + |(\hat{\Theta}_{j_2})_{p,q}|$  is consistent for  $|(\Theta_{j_1})_{p,q}| + |(\Theta_{j_2})_{p,q}|$ .

The condition for the combination of scales,  $\hat{\mathbf{G}}_{p,q} = 1$  iff  $(\hat{\Theta}_{j_1})_{p,q} \neq 0$  or  $(\hat{\Theta}_{j_2})_{p,q} \neq 0$  is equivalent to  $\hat{\mathbf{G}}_{p,q} = 0$  iff  $|(\hat{\Theta}_{j_1})_{p,q}| + |(\hat{\Theta}_{j_2})_{p,q}| = 0$ , and thus the scale combination procedure in Section 3.3 results in a consistent estimator of the  $\mathcal{CIG}$ . □

## B Simulation Study Results

In this section we include tables and plots to support the numerical results and conclusions discussed in Section 4. Section B.1 illustrates the different levels of sparsity in the estimated adjacency matrices for all simulated models. Section B.2 provides additional simulation study tables. Sections B.3–B.5 provide a direct comparison of how well each method recovers the adjacency matrix—and thus the underlying conditional independence graph—for the simulation studies in Section 4. In all cases, we display the true adjacency alongside the wavelet estimate and the best-performing Fourier-based alternative (Fourier- $\ell_1$  or Fourier- $\ell_2$ ). Each heatmap shows a grid of shaded squares indicating estimated adjacencies, with shading proportional to the frequency at which an edge is selected. The colour scale is shown in Figure B.1: black denotes edges always selected, and white denotes edges never selected.

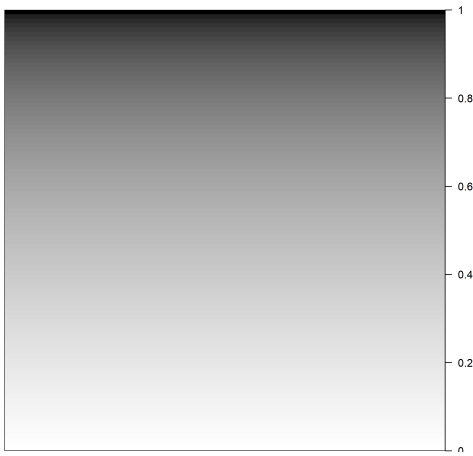


Figure B.1: Grayscale legend for the heatmaps in Figures B.2–C.25. A black square indicates that the edge is always selected and a white square indicates the edge is never selected.

## B.1 Sparsity of Simulated Models

Graph	Model		Estimated Sparsity, $\hat{\jmath}$	True Sparsity, $\jmath$
ER	10-dim GNAR(1,[1])	$\rho = 0.1$	8.0%	8.0%
		$\rho = 0.4$	82.72%	84.0%
ER	10-dim GNAR(2,[1,1])	$\rho = 0.1$	8.8%	8.0%
		$\rho = 0.4$	73.6%	84.0%
ER	25-dim GNAR(1,[2])	$\rho = 0.05$	19.1%	25.9%
		$\rho = 0.1$	49.4%	78.7%
Ring	10-dim GNAR(1,[1])	$\beta_{1,1} = 0.65$	42.5%	40.0%
		$\beta_{1,1} = 0.35$	31.5%	40.0%
Ring	25-dim GNAR(1,[1])	$\beta_{1,1} = 0.65$	20.6%	16.0%
		$\beta_{1,1} = 0.35$	20.4%	16.0%
	10-dim VAR(1)	$\beta_i \in I_1$	39.4%	40.0%
		$\beta_i \in I_2$	32.6%	40.0%
	10-dim VAR(1)		43.7%	44.0%
	20-dim VARMA(2,2)		20.0%	20.0%

Table B.1: Sparsity levels for the simulated models in Section 4. For each model, estimated sparsity is computed as the ratio of connections in the `WavTglasso` estimated adjacency matrix to the total number of possible connections, and the values are averaged across simulations.

## B.2 Additional Simulation Study Results

### GNAR Models on Erdős-Renyi (ER) Graphs

	$\rho = 0.1$			$\rho = 0.4$		
	TPR	FPR	TDR	TPR	FPR	TDR
W - $\ell_1$	<b>1</b>	<b>0.0057</b>	<b>0.9671</b>	<b>0.7833</b>	<b>0.1400</b>	<b>0.9687</b>
F - $\ell_1$ (glasso)	1	0.0739	0.5675	0.6633	0.0875	0.9766
F - $\ell_1$ (ADMM)	1	0.0391	0.7479	0.5514	0.0750	0.9740
F - $\ell_2$ (ADMM)	1	0.0157	0.8882	0.6043	0.1075	0.9684

Table B.2: True Positive, False Positive and True Discovery Rates for 10-dimensional GNAR(1,[1]) models over Erdős-Renyi graphs for  $T = 256$ . Values in bold identify the best method overall, considering aggregated TPR, FPR, and TDR values.

	$\rho = 0.1$			$\rho = 0.4$		
	TPR	FPR	TDR	TPR	FPR	TDR
W - $\ell_1$	<b>1</b>	<b>0.0023</b>	<b>0.9851</b>	<b>0.9110</b>	<b>0.1374</b>	<b>0.9806</b>
F - $\ell_1$ (glasso)	1	0.0287	0.7804	0.7610	0.0950	0.9776
F - $\ell_1$ (ADMM)	1	0.3174	0.2256	0.7752	0.1150	0.9733
F - $\ell_2$ (ADMM)	1	0.0035	0.9707	0.9862	0.3600	0.9360

Table B.3: True Positive, False Positive and True Discovery Rates for 10-dimensional GNAR(1,[1]) models over Erdős-Renyi graphs for  $T = 2048$ . Values in bold identify the best method overall, considering aggregated TPR, FPR, and TDR values.

	$\rho = 0.1$			$\rho = 0.4$		
	TPR	FPR	TDR	TPR	FPR	TDR
W - $\ell_1$	0.9950	0.0052	0.9620	<b>0.7338</b>	<b>0.0900</b>	<b>0.9789</b>
F - $\ell_1$ (glasso)	1	0.1609	0.3819	0.6690	0.0950	0.9755
F - $\ell_1$ (ADMM)	1	0.0822	0.5561	0.6443	0.0850	0.9782
F - $\ell_2$ (ADMM)	<b>1</b>	<b>0.0035</b>	<b>0.9680</b>	0.6524	0.0875	0.9767

Table B.4: True Positive, False Positive and True Discovery Rates for 10-dimensional GNAR(2,[1,1]) models over Erdős-Renyi graphs for  $T = 1024$ . Values in bold identify the best method overall, considering aggregated TPR, FPR, and TDR values.

	$\rho = 0.05$			$\rho = 0.1$		
	TPR	FPR	TDR	TPR	FPR	TDR
W - $\ell_1$	<b>0.6474</b>	<b>0.0110</b>	<b>0.9571</b>	<b>0.4954</b>	<b>0.0644</b>	<b>0.9660</b>
F - $\ell_1$ (glasso)	0.9830	0.0790	0.6518	0.3497	0.0298	0.9817
F - $\ell_1$ (ADMM)	0.4106	0.0004	0.9973	0.1461	0.0031	0.9943
F - $\ell_2$ (ADMM)	0.5081	0.0015	0.9924	0.4822	0.0947	0.9515

Table B.5: True Positive, False Positive and True Discovery Rates for 25-dimensional GNAR(1,[2]) models over Erdős-Renyi graphs for  $T = 1024$ . Values in bold identify the best method overall, considering aggregated TPR, FPR, and TDR values.

### GNAR Models on Ring Graphs

	$\beta = 0.65$			$\beta = 0.35$		
	TPR	FPR	TDR	TPR	FPR	TDR
W - $\ell_1$	<b>0.8770</b>	<b>0.0567</b>	<b>0.9202</b>	<b>0.5460</b>	<b>0.0680</b>	<b>0.8586</b>
F - $\ell_1$ (glasso)	0.7830	0.2640	0.6581	0.0870	0.0040	0.9960
F - $\ell_1$ (ADMM)	0.4950	0.0013	0.9969	0.1420	0	1
F - $\ell_2$ (ADMM)	0.6700	0.0400	0.9292	0.8800	0.5780	0.5199

Table B.6: True Positive, False Positive and True Discovery Rates for 10-dimensional GNAR(1,[1]) ring models for  $T = 1024$ . Values in bold identify the best method overall, considering aggregated TPR, FPR, and TDR values.

## VAR Models

	$I_1$			$I_2$		
	TPR	FPR	TDR	TPR	FPR	TDR
W - $\ell_1$	<b>0.9250</b>	<b>0.0633</b>	<b>0.9116</b>	<b>0.7730</b>	<b>0.0460</b>	<b>0.9250</b>
F - $\ell_1$ (glasso)	0.7720	0.2307	0.7005	0.7460	0.1987	0.7223
F - $\ell_1$ (ADMM)	0.4950	0.0047	0.9906	0.4440	0.0127	0.9731
F - $\ell_2$ (ADMM)	0.6550	0.0333	0.9401	0.5620	0.0080	0.9809

Table B.7: True Positive, False Positive and True Discovery Rates for VAR model, whose values of the coefficient matrix (17) are randomly picked in either of the intervals. Values in bold identify the best method overall, considering aggregated TPR, FPR, and TDR values.

## Bootstrapping

	$\rho = 0.1$			$\rho = 0.4$		
	TPR	FPR	TDR	TPR	FPR	TDR
$R = 1$	0.9500	0.0609	0.6781	0.6219	0.1550	0.9550
$R = 10$	0.9950	0.0122	0.9270	0.7557	0.1625	0.9613
$R = 50$	1	0.0057	0.9671	0.7833	0.1400	0.9687
$R = 100$	0.9900	0.0061	0.9616	0.7967	0.1700	0.9624
$\hat{\mathbf{S}}^{(X)}$	0.9950	0	1	0.8938	0.3175	0.9358

Table B.8: True Positive, False Positive and True Discovery Rates for 10-dimensional GNAR(1,[1]) models over Erdős-Renyi graphs for  $T = 256$  and with different number of bootstrap samples  $R$ ; (last row) WavTSglasso with corrected periodogram (4).

	$\rho = 0.1$			$\rho = 0.4$		
	TPR	FPR	TDR	TPR	FPR	TDR
$R = 1$	1	0.0035	0.9733	0.8724	0.1225	0.9747
$R = 10$	1	0.0052	0.9670	0.9157	0.0925	0.9811
$R = 50$	1	0.0065	0.9581	0.9110	0.0925	0.9806
$R = 100$	1	0.0065	0.9581	0.9133	0.0675	0.9861
$\hat{\mathbf{S}}^{(X)}$	0.9950	0.0667	0.9933	0.9986	0.3675	0.9347

Table B.9: True Positive, False Positive and True Discovery Rates for 10-dimensional GNAR(1,[1]) models over Erdős-Renyi graphs for  $T = 2048$  and with different number of bootstrap samples  $R$ ; (last row) **WavTSglasso** with corrected periodogram (4).

	$\beta = 0.65$			$\beta = 0.35$		
	TPR	FPR	TDR	TPR	FPR	TDR
$R = 1$	0.7260	0.0887	0.8552	0.5050	0.1513	0.7030
$R = 10$	0.7870	0.0573	0.9068	0.5410	0.0693	0.8579
$R = 50$	0.8770	0.0567	0.9202	0.5460	0.0680	0.8586
$R = 100$	0.8630	0.0400	0.9404	0.5370	0.0677	0.8672
$\hat{\mathbf{S}}^{(X)}$	0.8720	0.0667	0.9134	0.6510	0.1553	0.7621

Table B.10: True Positive, False Positive and True Discovery Rates for 10-dimensional GNAR(1,[1]) ring models with  $T = 1024$  and with different number of bootstrap samples  $R$ ; (last row) **WavTSglasso** with corrected periodogram (4).

### B.3 GNAR Models on Erdős-Renyi (ER) Graphs

#### B.3.1 10-dimensional GNAR(1,[1]) ER Models

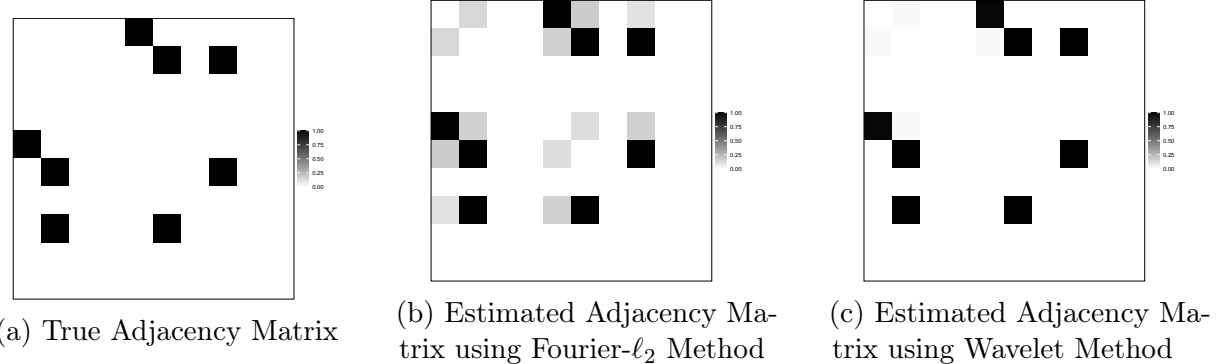


Figure B.2: True adjacency (a) and average estimated adjacencies using Fourier- $\ell_2$  (b) and wavelet- (c) TSglasso methods for the conditional independence graph of the 10-dimensional GNAR(1,[1]) model with  $\beta_{1,1} = 0.85$  on the ER graph with edge probability  $\rho = 0.1$ .

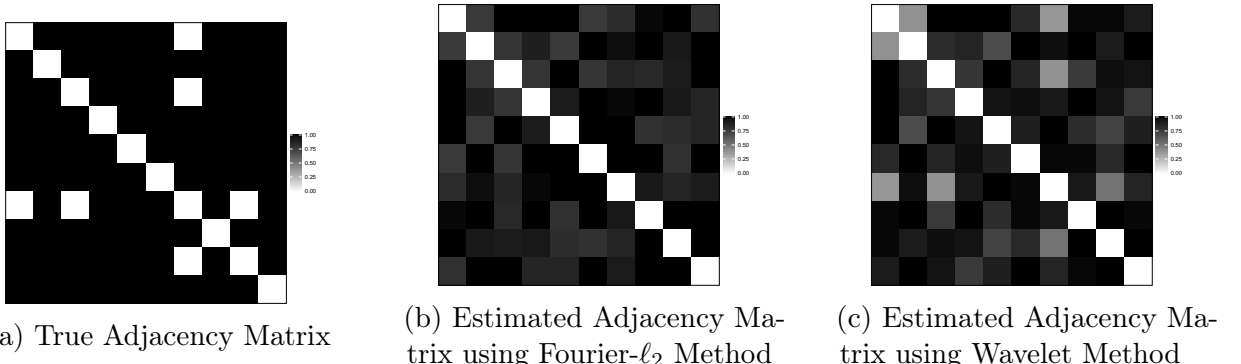


Figure B.3: True adjacency (a) and average estimated adjacencies using Fourier- $\ell_2$  (b) and wavelet- (c) TSglasso methods for the conditional independence graph of the 10-dimensional GNAR(1,[1]) model with  $\beta_{1,1} = 0.85$  on the ER graph with edge probability  $\rho = 0.4$ .

### B.3.2 10-dimensional GNAR(2,[1,1]) ER Models

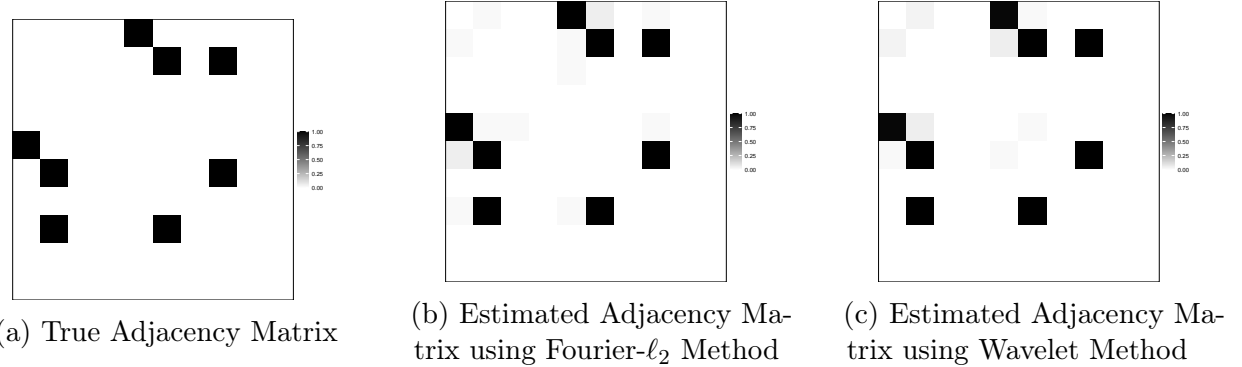


Figure B.4: True adjacency (a) and average estimated adjacencies using Fourier- $\ell_2$  (b) and wavelet- (c) TSglasso methods for the conditional independence graph of the 10-dimensional GNAR(2,[1,1]) model with  $\beta_{1,1} = \beta_{2,1} = 0.4$  on the ER graph with edge probability  $\rho = 0.1$ .

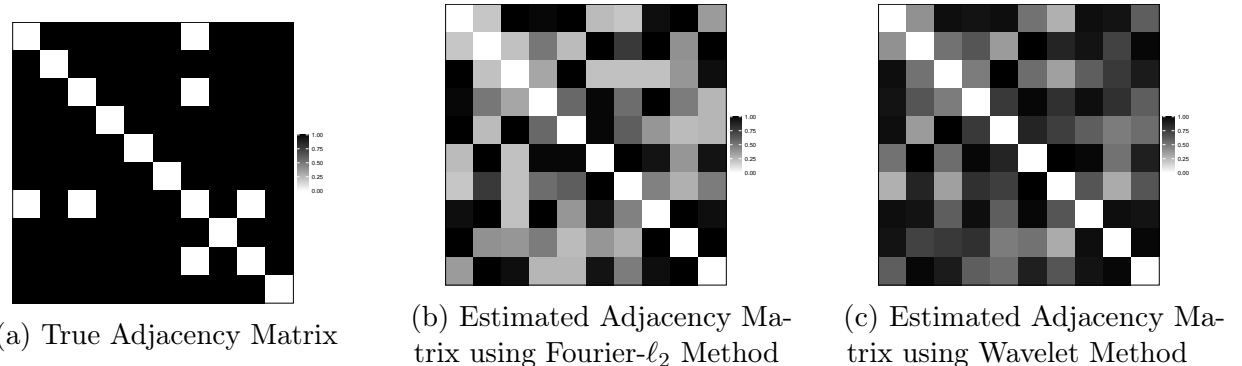


Figure B.5: True adjacency (a) and average estimated adjacencies using Fourier- $\ell_2$  (b) and wavelet- (c) TSglasso methods for the conditional independence graph of the 10-dimensional GNAR(2,[1,1]) model with  $\beta_{1,1} = \beta_{2,1} = 0.4$  on the ER graph with edge probability  $\rho = 0.4$ .

### B.3.3 25-dimensional GNAR(1,[2]) ER Models

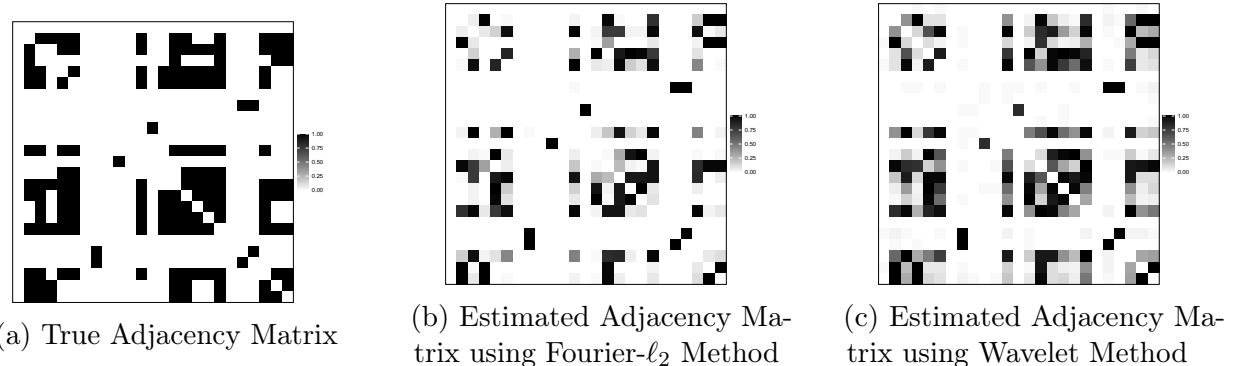
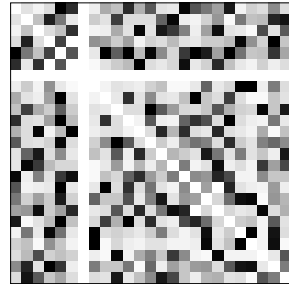


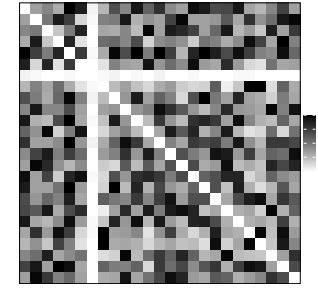
Figure B.6: True adjacency (a) and average estimated adjacencies using Fourier- $\ell_2$  (b) and wavelet- (c) TSglasso methods for the conditional independence graph of the 25-dimensional GNAR(1,[2]) model with  $\beta_{1,2} = \beta_{1,2} = 0.4$  on the ER graph with edge probability  $\rho = 0.05$ .



(a) True Adjacency Matrix



(b) Estimated Adjacency Matrix using Fourier- $\ell_2$  Method

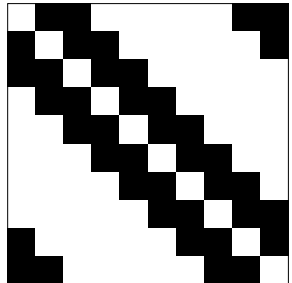


(c) Estimated Adjacency Matrix using Wavelet Method

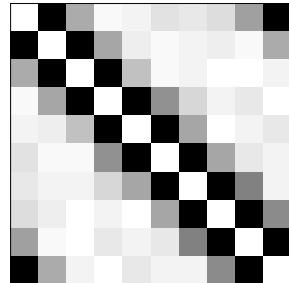
Figure B.7: True adjacency (a) and average estimated adjacencies using Fourier- $\ell_2$  (b) and wavelet- (c) TSglasso methods for the conditional independence graph of the 25-dimensional GNAR(1,[2]) model with  $\beta_{1,2} = \beta_{1,2} = 0.4$  on the ER graph with edge probability  $\rho = 0.1$ .

## B.4 GNAR Models on Ring Graphs

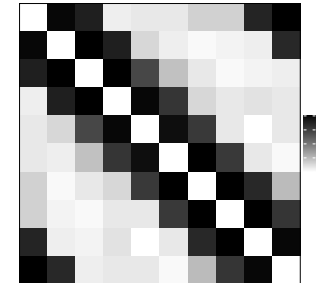
### B.4.1 10-dimensional GNAR(1,[1]) Ring Models



(a) True Adjacency Matrix

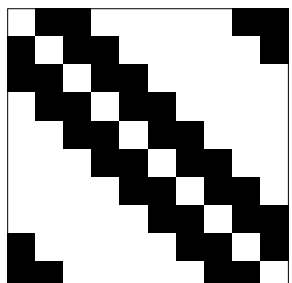


(b) Estimated Adjacency Matrix using Fourier- $\ell_2$  Method

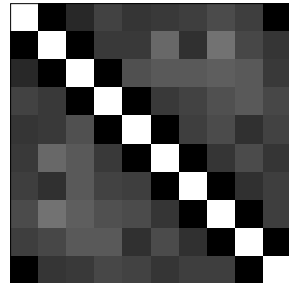


(c) Estimated Adjacency Matrix using Wavelet Method

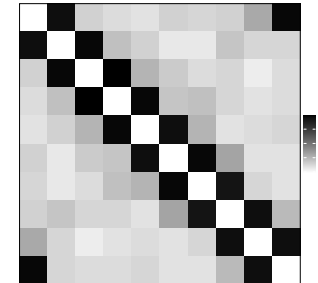
Figure B.8: True adjacency (a) and average estimated adjacencies using Fourier- $\ell_2$  (b) and wavelet- (c) TSglasso methods for the conditional independence graph of the 10-dimensional GNAR(1,[1]) model with  $\beta_{1,1} = 0.65$  on the Ring graph.



(a) True Adjacency Matrix



(b) Estimated Adjacency Matrix using Fourier- $\ell_2$  Method



(c) Estimated Adjacency Matrix using Wavelet Method

Figure B.9: True adjacency (a) and average estimated adjacencies using Fourier- $\ell_2$  (b) and wavelet- (c) TSglasso methods for the conditional independence graph of the 10-dimensional GNAR(1,[1]) model with  $\beta_{1,1} = 0.35$  on the Ring graph.

### B.4.2 25-dimensional GNAR(1,[1]) Ring Models

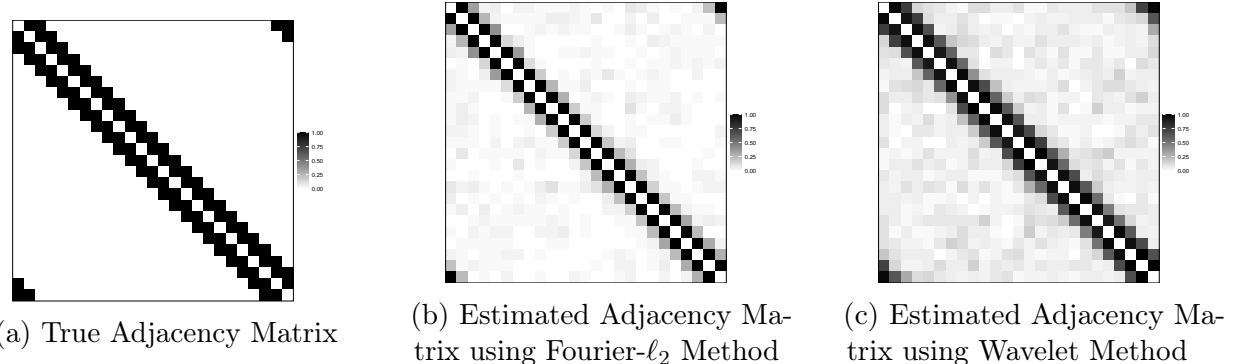


Figure B.10: True adjacency (a) and average estimated adjacencies using Fourier- $\ell_2$  (b) and wavelet- (c) TSglasso methods for the conditional independence graph of the 25-dimensional GNAR(1,[1]) model with  $\beta_{1,1} = 0.65$  on the Ring graph.

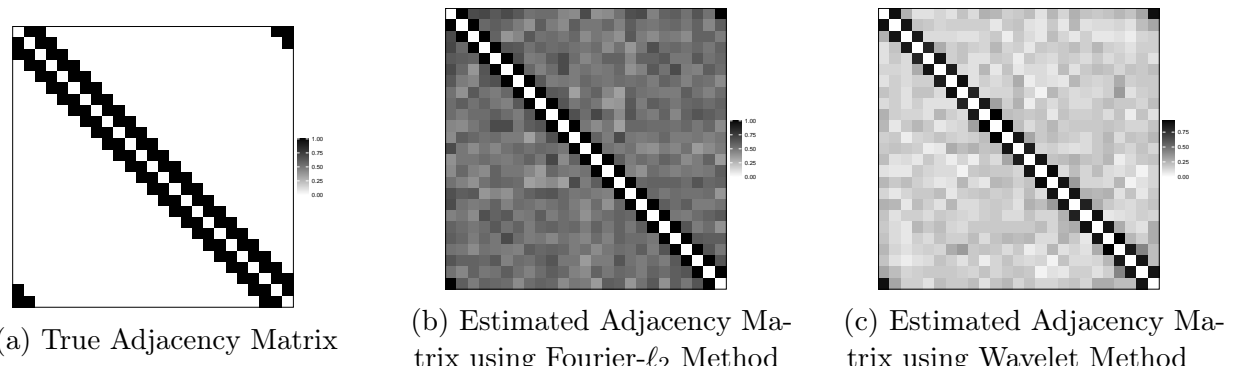
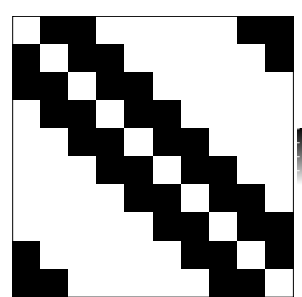


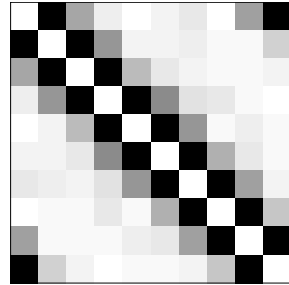
Figure B.11: True adjacency (a) and average estimated adjacencies using Fourier- $\ell_2$  (b) and wavelet- (c) TSglasso methods for the conditional independence graph of the 25-dimensional GNAR(1,[1]) model with  $\beta_{1,1} = 0.35$  on the Ring graph.

## B.5 VAR and VARMA Models

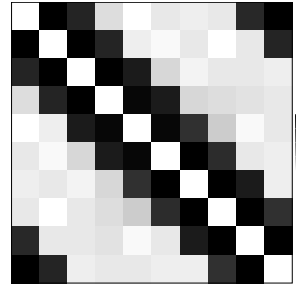
### B.5.1 10-dimensional VAR(1) with Varying Coefficient matrix $\mathbf{A}$



(a) True Adjacency Matrix

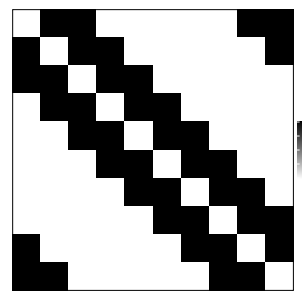


(b) Estimated Adjacency Matrix using Fourier- $\ell_2$  Method

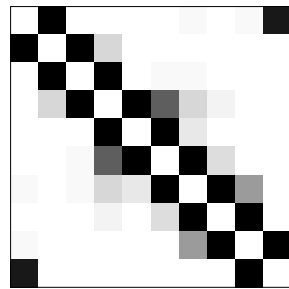


(c) Estimated Adjacency Matrix using Wavelet Method

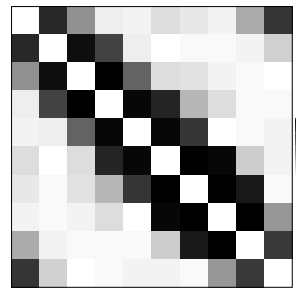
Figure B.12: True adjacency (a) and average estimated adjacencies using Fourier- $\ell_2$  (b) and wavelet- (c) TSglasso methods for the conditional independence graph of the 10-dimensional VAR(1) model with coefficient matrix  $\mathbf{A}$  in (17) with  $\beta_i \in I_1$ ,  $i = 1, \dots, 10$ .



(a) True Adjacency Matrix



(b) Estimated Adjacency Matrix using Fourier- $\ell_2$  Method



(c) Estimated Adjacency Matrix using Wavelet Method

Figure B.13: True adjacency (a) and average estimated adjacencies using Fourier- $\ell_2$  (b) and wavelet- (c) TSglasso methods for the conditional independence graph of the 10-dimensional VAR(1) model with coefficient matrix  $\mathbf{A}$  in (17) with  $\beta_i \in I_2$ ,  $i = 1, \dots, 10$ .

### B.5.2 10-dimensional VAR(1) and 20-dimensional VARMA(2,2) Model

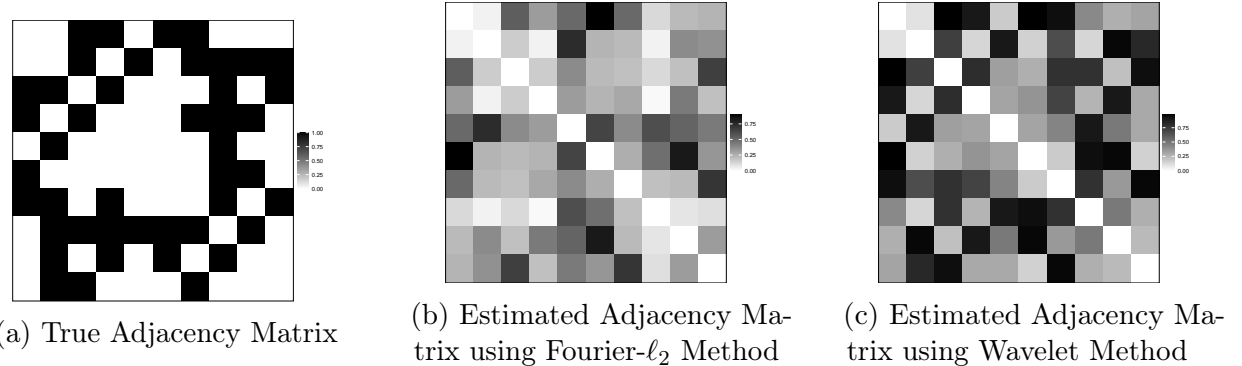


Figure B.14: True adjacency (a) and average estimated adjacencies using Fourier- $\ell_2$  (b) and wavelet- (c) TSglasso methods for the conditional independence graph of the 10-dimensional VAR(1) model with diagonal coefficient matrix  $\mathbf{A}$  and constraint noise precision matrix  $\Sigma_\epsilon^{-1}$ .

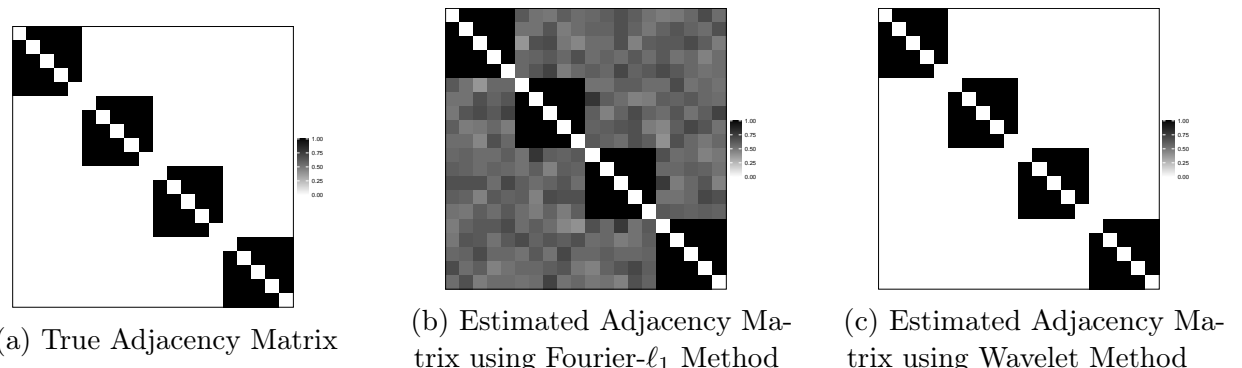


Figure B.15: True adjacency (a) and average estimated adjacencies using Fourier- $\ell_2$  (b) and wavelet- (c) TSglasso methods for the conditional independence graph of the 20-dimensional VARMA(2,2) model with block diagonal structure.

## C Underlying Graph Discovery Results

In this section we include plots to support the numerical results shown in Section 5. Sections C.2 and C.3 show plots of the true and estimated adjacency matrices using the clustering method as described in Section 5. Each heatmap are shown in a grayscale, with shading proportional to the frequency at which an edge is selected. The colour scale is shown in Figure B.1: black denotes edges always selected, and white denotes edges never selected.

### C.1 Additional Simulation Study Results

$\rho = 0.1$			$\rho = 0.4$		
TPR	FPR	TDR	TPR	FPR	TDR
0.9867	0	1	0.5411	0.0542	0.8730

Table C.11: True Positive, False Positive and True Discovery Rates for 10-dimensional GNAR(2,[1,1]) models over Erdős-Renyi graphs with  $T = 1024$ .

$\rho = 0.05$			$\rho = 0.1$		
TPR	FPR	TDR	TPR	FPR	TDR
0.5722	0.0314	0.5390	0.5677	0.0622	0.5211

Table C.12: True Positive, False Positive and True Discovery Rates for 25-dimensional GNAR(1,[2]) models over Erdős-Renyi graphs with  $T = 1024$ .

### C.2 GNAR Models on Erdős-Renyi (ER) Graphs

#### C.2.1 10-dimensional GNAR(1,[1]) ER Models

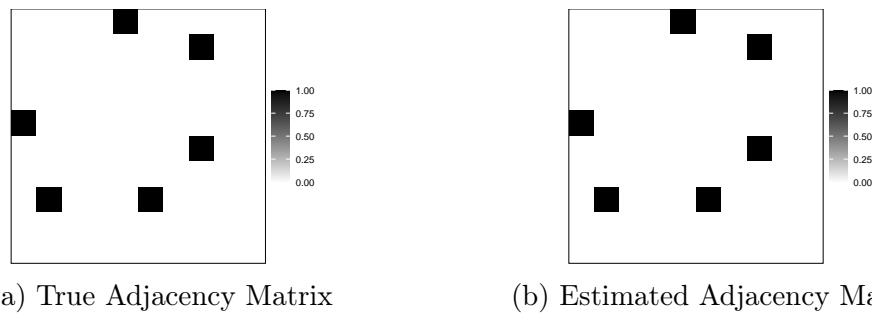
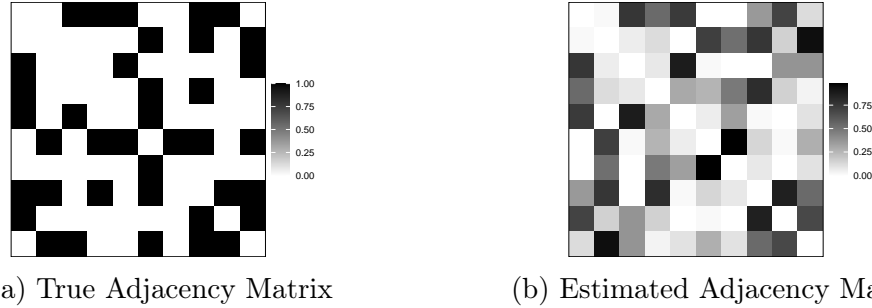


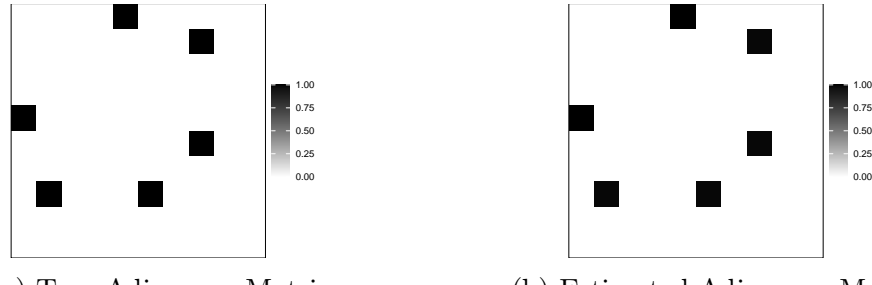
Figure C.16: True adjacency (a) and estimated adjacency (b) using the clustering method for recovering the underlying graph of the 10-dimensional GNAR(1,[1]) model with  $\beta_{1,1} = 0.85$  on the ER graph with edge probability  $\rho = 0.1$ .



(a) True Adjacency Matrix (b) Estimated Adjacency Matrix

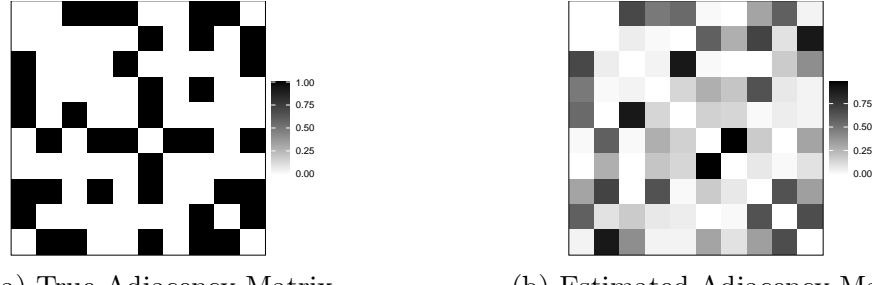
Figure C.17: True adjacency (a) and estimated adjacency (b) using the clustering method for recovering the underlying graph of the 10-dimensional GNAR(1,[1]) model with  $\beta_{1,1} = 0.85$  on the ER graph with edge probability  $\rho = 0.4$ .

### C.2.2 10-dimensional - GNAR(2,[1,1]) ER Models



(a) True Adjacency Matrix (b) Estimated Adjacency Matrix

Figure C.18: True adjacency (a) and estimated adjacency (b) using the clustering method for recovering the underlying graph of the 10-dimensional GNAR(2,[1,1]) model with  $\beta_{1,1} = \beta_{2,1} = 0.4$  on the ER graph with edge probability  $\rho = 0.1$ .



(a) True Adjacency Matrix (b) Estimated Adjacency Matrix

Figure C.19: True adjacency (a) and estimated adjacency (b) using the clustering method for recovering the underlying graph of the 10-dimensional GNAR(2,[1,1]) model with  $\beta_{1,1} = \beta_{2,1} = 0.4$  on the ER graph with edge probability  $\rho = 0.4$ .

### C.2.3 25-dimensional GNAR(1,[2]) ER Models

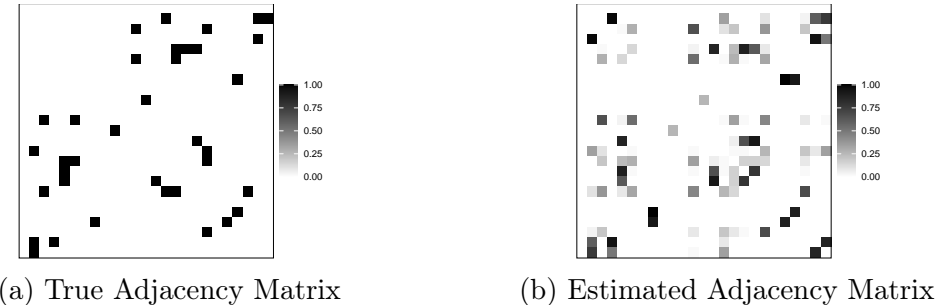


Figure C.20: True adjacency (a) and estimated adjacency (b) using the clustering method for recovering the underlying graph of the 25-dimensional GNAR(1,[2]) model with  $\beta_{1,1} = \beta_{1,2} = 0.4$  on the ER graph with edge probability  $\rho = 0.05$ .

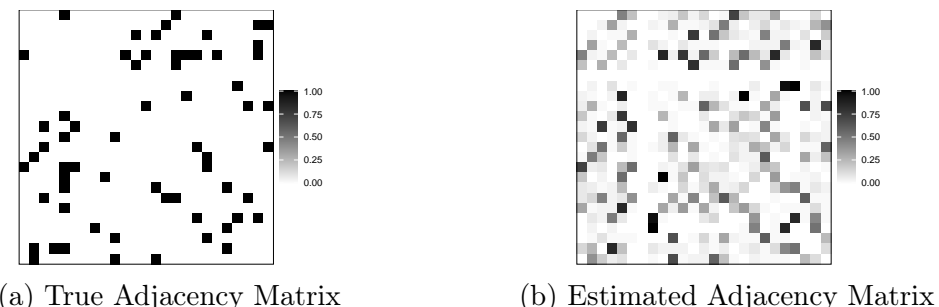


Figure C.21: True adjacency (a) and estimated adjacency (b) using the clustering method for recovering the underlying graph of the 25-dimensional GNAR(1,[2]) model with  $\beta_{1,1} = \beta_{1,2} = 0.4$  on the ER graph with edge probability  $\rho = 0.1$ .

## C.3 GNAR Models on Ring Graphs

### C.3.1 10-dimensional GNAR(1,[1]) Ring Models

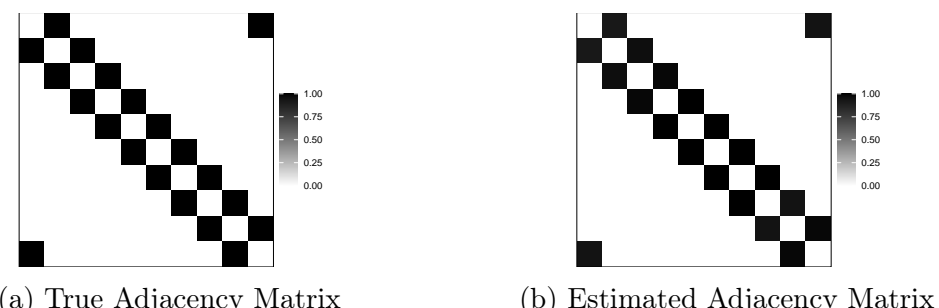


Figure C.22: True adjacency (a) and estimated adjacency (b) using the clustering method for recovering the underlying graph of the 10-dimensional GNAR(1,[1]) model with  $\beta_{1,1} = 0.65$  on the Ring graph.

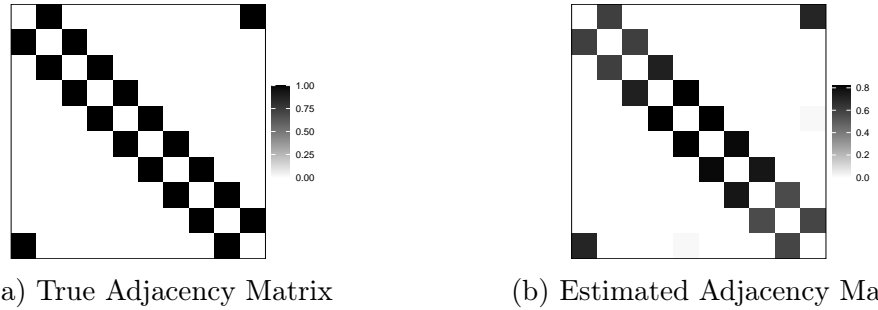


Figure C.23: True adjacency (a) and estimated adjacency (b) using the clustering method for recovering the underlying graph of the 10-dimensional GNAR(1,[1]) model with  $\beta_{1,1} = 0.35$  on the Ring graph.

### C.3.2 25-dimensional GNAR(1,[1]) Ring Models

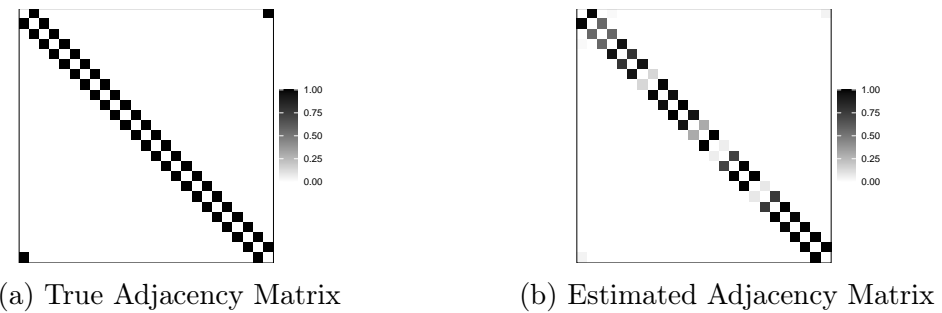


Figure C.24: True adjacency (a) and estimated adjacency (b) using the clustering method for recovering the underlying graph of the 25-dimensional GNAR(1,[1]) model with  $\beta_{1,1} = 0.65$  on the Ring graph.

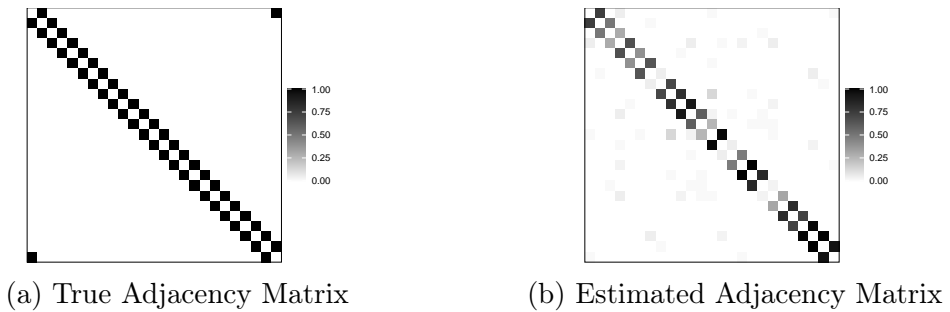


Figure C.25: True adjacency (a) and estimated adjacency (b) using the clustering method for recovering the underlying graph of the 25-dimensional GNAR(1,[1]) model with  $\beta_{1,1} = 0.35$  on the Ring graph.

## D COVID-19 Data Information

NHS England Region	Nodes
NHS England Cumbria and North East	1-4
NHS England Yorkshire and Humber	5-12
NHS England Cheshire and Merseyside	13-18
NHS England Greater Manchester	19-23
NHS England Lancashire	24-26
NHS England North Midlands	27-31
NHS England Central Midlands	32-32
NHS England West Midlands	33-39
NHS England East	40-47
NHS England London	48-64
NHS England South West (South West North)	65-67
NHS England South East (Kent, Surrey and Sussex)	68-74
NHS England South West (South West South)	75-77
NHS England South East (Hampshire, Isle of Wight, Thames Valley)	78-81

Table D.13: 14 different NHS England Trust regions and their corresponding nodes in the network after preprocessing steps.